REVIEW　　　　　　　　　　　　　　　　　　　　　　　　**Open Access**

Post-sunset rise of equatorial *F* layer—or upwelling growth?

Roland T. Tsunoda[1*], Susumu Saito[2,3] and Trang T. Nguyen[4]

Abstract

According to the so-called upwelling paradigm, development of equatorial plasma bubbles (EPBs) involves (1) appearance of an upwelling (i.e., local uplift with a zonal width of ~ 400 km) in the bottomside of the equatorial *F* layer, (2) its growth via the *F*-region interchange instability during the post-sunset rise (PSSR) of the *F* layer, and (3) launching of EPBs, which starts near the end of PSSR, from within the confines of the upwelling. In this description, the PSSR is presumed to be the primary driver of the paradigm, with upwelling growth dependent on PSSR strength. As constructed, the paradigm describes EPB development when PSSR is strong (i.e., high solar activity), but not when it is weak. We, show, for the first time, that when PSSR is weak (e.g., low solar activity), upwelling growth can still be comparable in strength to what would be considered a strong PSSR, and that this growth drives EPB development. Given that EPBs do not develop outside of upwellings, regardless of solar activity, we are led to conclude, against mainstream thinking, that the controlling driver for EPB development is upwelling growth, not PSSR. For continued progress toward understanding EPB development, a crucial next step is to identify the source mechanism for upwelling growth, especially when PSSR is weak, and to better understand the complexities of the underlying physics.

Keywords: Equatorial plasma bubbles, Equatorial spread *F*, Day-to-day variability, Post-sunset rise of equatorial *F* layer, Large-scale wave structure, Upwelling paradigm, Upwelling growth, Pre-reversal enhancement, Electric field, Equatorial ionosphere

Introduction
Overview

The post-sunset rise (PSSR) of the equatorial *F* layer is a familiar feature of the low-latitude ionosphere; it can be seen in ionospheric measurements (e.g., Tsunoda and White, 1981), and is reproducible with global-scale electrodynamical models (e.g., Batista et al. 1986; Eccles, 1998a, b; Fesen et al. 2000; Rodrigues et al. 2012; Richmond et al. 2015). The PSSR is interesting because the process is complex, involving no fewer than three contributing mechanisms (Rishbeth, 1971; Eccles, 1998a; Farley et al. 1986; Haerendel and Eccles, 1992; Eccles et al. 2015; Richmond et al. 2015). Interest in PSSR is widespread for various reasons, but largely because it appears to control development of plasma structure in the nighttime equatorial *F* layer, generically referred to as equatorial spread *F* (ESF) (e.g., Clemesha and Wright, 1966;

Fejer et al. 1999). We are most interested, herein, in one form of ESF, equatorial plasma bubbles (EPBs), which are initiated in the bottomside of the equatorial *F* layer, with upward development into the topside ionosphere.

The fundamental process for EPB development is thought to be the generalized gradient-drift (or Rayleigh-Taylor) instability (e.g., Tsunoda and White, 1981; Kelley et al. 1981), hereafter, referred to simply as the interchange instability. Only a linear form of this instability is needed to infer a relationship between PSSR and bottomside ESF (e.g., Dungey, 1956; Farley et al. 1970), but computer simulations that are based on nonlinear formulations of the instability were needed to demonstrate linkage between PSSR and EPBs in the topside *F* layer (e.g., Scannapieco and Ossakow, 1976; Zalesak and Ossakow, 1980; Zalesak et al. 1982).

When viewed climatologically, the experimental evidence, supporting PSSR control of EPB (and ESF) development, is strong (e.g., Clemesha and Wright, 1966; Tsunoda, 1985; Fejer et al. 1999; Gentile et al. 2006; Su et al. 2008). Questions arise, however, when the

* Correspondence: roland.tsunoda@sri.com
[1]Center for Geospace Studies, SRI International, 333 Ravenswood Ave., Menlo Park, California 94025, USA
Full list of author information is available at the end of the article

Tsunoda *et al. Progress in Earth and Planetary Science* (2018) 5:22

Page 2 of 28

PSSR-to-ESF relationship is evaluated with shorter time scales, such as on a day-to-day (D2D) basis. Indeed, up close, the PSSR does not display clear causal control of ESF occurrence. For example, when PSSR and ESF are monitored from a single location, correlation may appear to be present on a D2D basis, but the scatter is usually large (e.g., Abdu et al. 1983; Fukao et al. 2006; Saito and Maruyama, 2006, 2007).

The most glaring indicator, that something must be wrong with the interpretation of D2D variability, in terms of a simple PSSR-to-ESF relationship, is the finding that the PSSR, measured over one location, cannot be used to reliably predict ESF occurrence over another nearby location (e.g., Tsunoda, 2005; Saito and Maruyama, 2007; Tsunoda et al. 2010). We believe this inability to forecast ESF with one-station measurements points to a D2D variability that is intertwined with longitudinal variability (e.g., Tsunoda and White, 1981, Tsunoda, 2005, 2015; Saito and Maruyama, 2007). This longitudinal variability cannot be ignored because the zonal decorrelation distance turns out to be as short as a few hundred kilometers, which means even regional forecasting becomes a futile endeavor. As discussed, herein, we suggest that longitudinal decorrelation is caused by control imposed by an upwelling (i.e., a local uplift), which develops in the bottomside of the equatorial F layer (e.g., Tsunoda and White, 1981; Saito and Maruyama, 2007; Tsunoda, 2015).

In this paper, we address questions generally regarding the D2D/longitudinal variability problem, and more specifically, the roles and processes that produce vertical plasma-transport over the magnetic dip equator. Because F-region plasma is essentially incompressible in a plane transverse to the geomagnetic field (B), vertical transport is produced by a zonal electric field (E). We consider two observed forms of upward transport, the PSSR and upwelling growth, and their sources. In addition to the pre-reversal enhancement (PRE) of dayside E, which is responsible for PSSR, we consider a role played by a polarization E, which accompanies an upwelling in the bottomside of equatorial F layer. The notion that this polarization E should be additive to the PRE E is not new (Tsunoda, 2005; Tsunoda and Ecklund, 2007); what is new and unexpected is our finding that the polarization E can not only be strong, that is, comparable to what we consider to be a strong PRE, but this can also occur when the PRE E is actually weak! (see "Case Study: 27 March 2006" section) Deeply modulated upwellings have been observed before [e.g., Tsunoda (2015)], but they apparently have not been commonplace enough to warrant immediate consideration regarding whether upwelling growth competes with the PSSR for control of upward transport and EPB development.

Organization of paper

The contents are presented in five sections. Background material can be found in the "Introduction" section. In the remainder of this section, we describe the basic electrodynamics around sunset ("Electrodynamics around sunset"), mainly to differentiate the PSSR, which is a global-scale process, from upwelling growth, which is a local-scale process. The difference in scales is such that the first is an order-of-magnitude greater than the second. In fact, given this huge difference, upwelling growth should appear to be superposed on the PSSR (as shown in the "Electrodynamics around sunset" section). We also briefly discuss what is known about how PSSR, upwelling growth, and ESF (or EPBs) are related, namely, in terms of two hypotheses, the PSSR-to-ESF paradigm and the upwelling paradigm ("EPB development: two paradigms"). We then hypothesize that the D2D variability is related causally to variability (in space and time) associated with the local-scale process ("'PSSR' = PSS + upwelling growth"), rather than only with the global-scale process.

The findings that support our hypothesis are presented in two parts: (1) related results, which we have extracted from various studies ("Findings of related interest"), and (2) new findings, which we have deduced from a case study ("Case study: 27 March 2006"). We first show ("Nature of h'F(2.5) curves") that the measured upward-transport of the bottomside F layer can be substantially different, when measured at two closely spaced ionosonde locations, Chumphon (CPN) and Bac Lieu (BCL). Using scale-size arguments ("Electrodynamics around sunset"), we further hypothesize that the observations can be interpreted in terms of an upwelling. We then validate our hypothesis by answering four questions (Q1 through Q4), which are posed in the "Q1: Was PSSR behavior as expected?" section through "Q4: Other EPBs and upwellings?" section. A sketch of an upwelling-growth model, which is consistent with observations, is presented in the "Upwelling growth model" section.

To provide a perspective view of our findings, we compare our findings with results from Kodaikanal (Sastri, 1998) in the "Our case study: extreme event?" section. Those results are summarized and discussed in the "Discussion" section. Two key conclusions could be drawn from this study ("Conclusions"): (1) strong upwelling growth occurs, even in the presence of a weak PSSR, and it appears to play an important role in EPB development; and (2) there is crucial need to identify and understand the basic mechanisms that are responsible for strong upwelling growth during weak PSSR.

Electrodynamics around sunset
PSSR: global-scale process
The PSSR of the equatorial F layer is a well-established feature in global, low-latitude electrodynamics [e.g., see review by Heelis (2004)]. The lifting of the F layer is produced by an enhancement of the dayside, eastward E, just prior to its reversal to the nighttime, westward direction. As discussed

Tsunoda *et al. Progress in Earth and Planetary Science* (2018) 5:22

Page 3 of 28

in more detail in the "Overview" section, the primary sources for the PRE appear to have been identified (e.g., Eccles et al. 2015; Richmond et al. 2015), and the PSSR appears reproducible with global models, which assume that vertical gradients are much steeper than longitudinal gradients. With this assumption, local time (LT) becomes interchangeable with longitude (e.g., Batista et al. 1986; Eccles, 1998a; Fesen et al. 2000; Rodrigues et al. 2012; Richmond et al. 2015). If we then note that the observed duration of the PSSR is typically 2 h (e.g., Fejer et al. 1991), this implies that the PRE extends over 30° in longitude, which is more than 3000 km in zonal distance (e.g., Saito and Maruyama, 2007). This estimate is consistent with Huang and Kelley (1996b), who used a quasi-Gaussian-shaped pulse waveform for E with a 2000 km full width at half maximum, for their modeling studies of EPB development.

Given that the PSSR starts at a fixed LT, for a given longitude, and that the initiation point for the PSSR sweeps westward with the solar terminator, a tilt in isodensity contours should appear in the bottomside F layer with contours higher in the east. And, indeed, this tilt has been measured with ALTAIR, a fully steerable incoherent-scatter (IS) radar (Tsunoda et al. 1979), by performing east-west spatial-scans of the F layer around sunset (e.g., Tsunoda and White, 1981). Examples of a tilted F layer, associated with
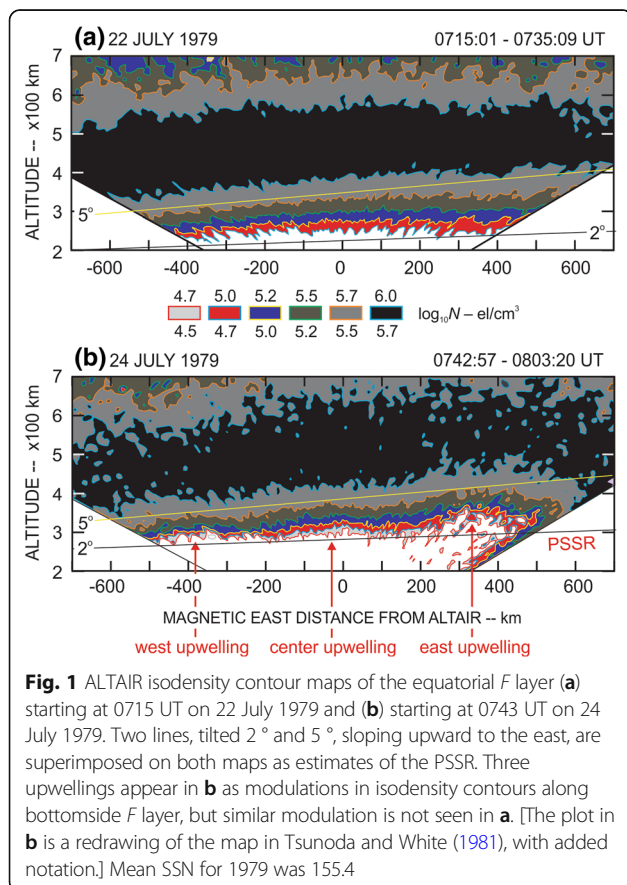
the PSSR, are presented in Fig. 1. Figure 1b is a redrawing of an ALTAIR isodensity contour map, which was first presented in Tsunoda and White (1981). We have drawn two sloping lines in each of the maps, with tilts of 2° and 5°, which can be compared with the mean tilts in isodensity contours near the base of the F layer and closer to the peak of the F layer. Not only are they similar, the tilted regions extend across the entire scanned sector, 1200 km in zonal extent, which is consistent with the spatial scale of the PSSR in global models. The increasing tilt in the straight lines with altitude suggests presence of a positive height gradient in PSSR rate; similar results were reported by Sastri et al. (1995) for the Indian sector during December solstice 1994.

Upwelling: a local-scale process

A less-established feature that also participates actively in the electrodynamics of the equatorial F layer is an upwelling (Tsunoda and White, 1981; Tsunoda, 2005, 2015; Tsunoda and Ecklund, 2007). Examples of three upwellings can be seen in Fig. 1b, in the form of altitude-modulated isodensity contours along the base of the F layer. [When they appear as a quasi-periodic wave train, they are referred to as large-scale wave structure (LSWS).] Upwellings have been observed, for example, with all-sky imagers and scanning photometers of 630 nm emissions (e.g., Weber et al. 1978, 1996; Patra et al. 2013), and in the form of variations in total electron content (TEC), using a radio-beacon satellite in a low-inclination orbit (e.g., Thampi et al. 2009; Tsunoda et al. 2010; Tulasi Ram et al. 2012). We have included Fig. 1a to show that modulation similar to that in Fig. 1b is not ubiquitous, despite presence of a significant PSSR on both nights.

An upwelling is often thought of by others to be a passive seed perturbation that does not alter the electrodynamics of the background ionosphere (e.g., Weber et al. 1978, 1996; Fagundes et al. 1999; Li et al. 2012; Narayanan et al. 2012; Patra et al. 2013). Instead, an upwelling, with a zonal extent of say, 400 km, actually grows in amplitude during the PSSR, often exceeding 100 km (e.g., Tsunoda, 2015). As just mentioned, upwelling-growth is thought to be produced by an eastward E, which has the zonal dimension of the upwelling.

The LSWS-scale zonal E should be associated a divergent, eastward Pedersen-current in the bottomside of the equatorial F layer (see "Strength of 'seed' plasma perturbations" section). There are two possible sources of divergence, a zonal variation either in the outward component of the meridional neutral wind (U) that is transverse to B, or in the field-line-integrated Pedersen conductivity of the F layer (Σ_P^F). The perturbation in U (i.e., ΔU) could be associated with an atmospheric gravity wave (AGW), and a polarization E would appear to maintain current continuity in the background Pedersen current. Plasma transport would have $E \times B$ motion, but the plasma

Fig. 1 ALTAIR isodensity contour maps of the equatorial F layer (**a**) starting at 0715 UT on 22 July 1979 and (**b**) starting at 0743 UT on 24 July 1979. Two lines, tilted 2 ° and 5 °, sloping upward to the east, are superimposed on both maps as estimates of the PSSR. Three upwellings appear in **b** as modulations in isodensity contours along bottomside F layer, but similar modulation is not seen in **a**. [The plot in **b** is a redrawing of the map in Tsunoda and White (1981), with added notation.] Mean SSN for 1979 was 155.4

Tsunoda *et al. Progress in Earth and Planetary Science* (2018) 5:22

Page 4 of 28

density (N) would not become perturbed unless there is a vertical gradient in the background N (i.e., ∇N) profile.

If the background Pedersen current is zero, upwelling growth would depend entirely on ΔU and the interaction time between AGW and the bottomside F layer (e.g., Röttger, 1976; Klostermeyer, 1978; Huang and Kelley, 1996a, b; Tsunoda, 2010b, c). On the other hand, if there is a background eastward Pedersen-current, the process becomes the interchange instability, which would be the same as that for EPBs ("EPB development: two paradigms"). The fact that this process is unstable (in the presence of an upward-directed ∇N), as discussed below, supports the possibility that this polarization E could grow rapidly, whereas the E responsible for the PSSR should be a stable, well-behaved process (see "Upwelling growth: weak PSSR" section). Given that the polarization E and PRE E are additive within the upwelling, the total E therein is always larger than the PRE E.

EPB development: two paradigms

There are two paradigms that describe EPB development in the nighttime equatorial F layer: the PSSR-to-ESF paradigm and the upwelling paradigm. The basis for both is the interchange instability ("Overview"). That is, the bottomside of the equatorial F layer, with its upward-directed ∇N, is unstable in the presence of an eastward Pedersen current (as mentioned previously). An upward perturbation (in isodensity contours) produces a local conductivity that is lower than that of the background. An eastward polarization E appears within the local depletion to preserve current continuity. At the same time, the eastward E acts to further increase upward transport, which further lowers conductivity; hence, the process is unstable. The fundamental difference between the two paradigms is the nature of the assumed upward ∇N region. In the PSSR-to-ESF paradigm, horizontal extent in longitude is assumed to be infinite, which means the process is thought to be one dimensional (1D), with variations that are dependent only on altitude. In the upwelling paradigm, the zonal width of an upwelling reflects the longitudinal extent of the process. This means that with upwelling growth, the depth of altitude modulation can be comparable to the width of an upwelling in longitude. The upwelling paradigm not only accommodates two-dimensional (2D) effects, it describes in detail how ESF and EPBs are expected to develop.

PSSR-to-ESF paradigm

This paradigm continues to have appeal because ESF (and EPB) are correlated with a high PSSR, when evaluated climatologically (e.g., Clemesha and Wright, 1966; Tsunoda, 1985; Fejer et al. 1999; Gentile et al. 2006; Su et al. 2008). This paradigm breaks down, however, when evaluated using shorter time scales, such as on a D2D

basis. The major flaw of this paradigm is that it predicts EPB occurrence with only PSSR strength as its primary driver. The linearized growth rate of the interchange instability, which is presumed to contain all the physics, is usually tweaked by allowing variations in the bottom-side ∇N, or in Σ_P^F; the change in Σ_P^F can be produced by a meridional U, which alters the hemispheric distribution of N (e.g., Maruyama, 1996; Saito and Maruyama, 2006; Maruyama et al. 2008, 2009). [Without measurements of the ion-neutral collision frequency or neutral density, they are usually assumed to remain unchanged. Causal and feedback effects of the neutral gas and plasma (e.g., Schunk and Demars, 2003) remain to be investigated.] There is growing appreciation, however, for the possibility that variability in seed amplitude could also be a factor in the development of EPBs, especially in situations, when PSSR strength is not strong (e.g., Röttger, 1977, 1981; Aarons, 1993; McClure et al. 1998: Ogawa et al. 2006; Patra et al. 2013; Tsunoda et al. 2015; Abdu et al. 2015; Su et al. 2014; Li et al. 2016).

This 1D paradigm does not provide a means by which to understand the features observed in ESF. For example, ESF occurs in patches (e.g., Röttger, 1973; Tsunoda, 2015), and EPBs appear in isolated clusters (e.g., Tsunoda and White, 1981; Singh et al. 1997). In contrast, the PSSR-to-ESF paradigm essentially forecasts a continuous distribution of ESF and EPBs, because it assumes a horizontally stratified F layer, which must structure (not structure) everywhere, when PSSR is strong (weak). To explain the appearance of ESF in patches (and EPBs in clusters), some form of seeding must be assumed without understanding the causal physics.

Upwelling paradigm

In contrast, this paradigm provides a step-by-step description, namely, appearance of a seed upwelling perturbations in the late afternoon, amplification occurring around E-region sunset (SS_E), and development of EPBs. Patches of ESF and clusters of EPBs can be explained in terms of structure development within the confines of preexisting upwellings (e.g., Tsunoda and White, 1981; Singh et al. 1997; Eccles, 2004). Of particular interest here, are the following features of this paradigm: (1) appearance of seed upwellings prior to SS_E, (2) upwelling growth around SS_E, (3) absence of EPB development until SS_B (4) appearance of first (primary) EPB near the crest of upwelling (Tsunoda and White, 1981), and (5) subsequent appearance and growth of secondary EPBs along the west wall of the upwelling (Tsunoda, 1983, 2015). Upwelling growth and primary-EPB development are thought to be driven by the interchange instability with PSSR as the driver. Secondary EPBs are also thought to be produced by the interchange

Tsunoda *et al. Progress in Earth and Planetary Science* (2018) 5:22

Page 5 of 28

instability, but with an eastward U, blowing through the west wall of an upwelling, as the main driver for this secondary process. This repeatable sequence of events, which occurs inside (but not outside) of an upwelling, is referred to as the upwelling paradigm (Tsunoda, 2015).

D2D variability

The upwelling paradigm is appealing because the details found in its envisioned scenario for EPB development contain the elements that could be responsible for the so-called D2D variability. Besides a dependence on PSSR strength, other possible factors include (1) a possible D2D variability in seeding, and (2) a variability in whether an upwelling has been imprinted onto the bottomside of the equatorial F layer by the time of SS_F. An EPB would likely be launched at a longitude where SS_F intercepts an upwelling. According to the upwelling paradigm (Tsunoda, 2015), the upwelling, which appears around sunset, is nearly stationary in longitude, during its early growth phase. In other words, where EPBs develop is specified by the location of the upwelling around SS_E. Once generated, EPBs drift eastward, together with the upwelling, which occur during the late growth phase and the descent of the F layer. This scenario is intriguing because the apparent D2D variability could be associated with (1) the nature of the seed, (2) the strength of the PSSR, (3) the nature of upwelling growth, and (4) the zonal drift of upwellings and EPBs during the course of the night. The overall objective of this paper is to examine these possibilities.

'PSSR' = PSSR + upwelling growth

From the discussion in the "Electrodynamics around sunset" section, the PSSR and upwelling growth must each be produced by a separate, eastward E. This means the measured upward-transport velocity must be the sum of those two components, as suggested previously (Tsunoda, 2005, 2015; Tsunoda and Ecklund, 2007; Saito and Maruyama, 2007). Hence, the measured (or apparent) upward displacement ('PSSR') is the sum of PSSR and upwelling growth. If this is the case, either D2D or longitudinal variability, or both, could be the source of scatter found in 'PSSR' observations. Unfortunately, the task of sorting the two contributions is not straightforward because there is a paucity of instruments that can detect an upwelling and measure its growth.

The difficulty arises from the fact that an upwelling is virtually stationary in the zonal direction during its early growth phase (e.g., Tsunoda and White, 1981; Fagundes et al. 1999), which occurs around SS_E. All-sky imagers have been used to monitor the distribution of 630 nm emissions (e.g., Weber et al. 1978, 1996), but observations were usually made after the PSSR, during the descent of the F layer, when the signal-to-noise ratio (SNR) relatively

high. Encouragingly, wavelike structures have recently been detected with a 630 nm scanning photometer at Gadanki (6.5°N magnetic latitude) before SS_B and found to be associated with EPBs, as detected with the Gadanki radar (Patra et al. 2013). While promising, spaced photometers and tomographic inversion may be needed to extract altitude information.

For instruments, that make only overhead measurements versus time (e.g., radar, ionosonde), spatial structure can be detected only if that structure is moving horizontally. This means an upwelling would not be discernible during its early growth phase, but it would become detectable when the upwelling grows in amplitude and enters the region of eastward drift. Alternatively, spatial structure can be detected by using two or more instruments that are closely spaced in longitude. With this setup, spatial information can be extracted from differences in measured properties between pairs of instruments.

Another approach (used herein) is to take advantage of the clear disparity in zonal scales, between PSSR and upwelling, to extract the contributions to 'PSSR.' That is, if estimates of 'PSSR' are the same, when measured by ionosondes spaced in longitude, the estimate of 'PSSR' is likely to be that of PSSR-only, and that an upwelling was not present. But, if the estimates are different, the smaller of the two is likely to be that of PSSR and the difference in estimates would likely be that of upwelling growth.

Findings of related interest

In the following six subsections (i.e., "Jicamarca radar and Huancayo ionosonde" through "Three oonosondes and TEP experiment"), we review and synthesize results from other studies, which pertain to spatial variability in either vertical displacement or transport velocity associated with the bottomside of the equatorial F layer. The spatial scales of interest are those that are typically associated with LSWS. These results were obtained by ground-based instruments (radar, ionosonde, oblique-incidence radio-propagation link), operated in pairs or clusters, or by low-altitude, Earth-orbiting satellites (carrying in situ probes or radio beacon) in low-inclination orbits. The results are presented, more or less, in chronological order; relevant findings are summarized together with those from this study in the "Summary of findings" section.

Jicamarca radar and Huancayo ionosonde

The earliest simultaneous measurements of 'PSSR' from two closely spaced locations in longitude were made with an IS radar at Jicamarca (JIC), and an ionosonde at Huancayo (HUA). These stations are separated by only 1.6° in longitude (Table 1). Rastogi (1978) presented one example (26 April 1971) in which he compared the upward transport velocity ($V_z F$), measured with the IS radar, to the minimum virtual height ($h'F$) versus LT,

measured with the ionosonde. Rastogi ([1978](#)), however, chose not to compare short-period variations because measurements were not collocated.

Upwellings and radar plumes

The most relevant results on LSWS, using the JIC radar and HUA ionosonde, were reported by Kelley et al. ([1981](#)), which appeared soon after the ALTAIR results on LSWS were reported by Tsunoda and White ([1981](#)). We mention the latter results here because both are case studies from 1979, a year of high solar activity, and the observed features are quite similar. Results from ALTAIR (e.g., Fig. [1](#)), however, were derived from a temporal sequence of fully 2D spatial scans, which eliminated space-time ambiguities in interpretation. Hence, a comparison of results should shed light on the validity of interpretation that is based on spaced-station observations. The results from Kelley et al. ([1981](#)) are presented in Fig. [2](#). Here, we have combined their radar measurements, which are shown as an altitude-time-intensity (ATI) plot of radar backscatter (grayscale), with that of $h'F$ versus LT, which is drawn with red circles (white fill) connected by red line segments.

On this night of spectacular activity (21 March 1979), there appeared what could be called two giant oscillations in the ATI plot, with crests occurring around 1945 and 2125 LT. These temporally measured features turn out to be consistent with the upwelling paradigm, if we envision these structures to be slowly developing as they drift eastward. In this case, the oscillations are interpreted as two upwellings, as marked (and labeled) by the large upward-pointing arrows. There are backscatter 'plumes' associated with the crests, and those with the 'descending'

side of each oscillation; the descending side would be the west wall of an upwelling. The plumes have been shown to be spatially collocated with upward-extending EPBs (Tsunoda, [1980](#), [1981](#)).

That is, we interpret the oscillations to be LSWS, in which the crests would be collocated with upwellings. Once an upwelling grows in amplitude, primary EPBs would be launched from the crest of the upwelling followed by the development of secondary EPBs along the west wall of the upwelling. We can see that this was indeed the case, on this night; backscatter plumes, which are collocated with EPBs (Tsunoda, [1980](#), [1981](#)), did appear as described, if we keep in mind that the upwellings drift eastward (after their early growth phase), which means the 'descending' side is the west wall. In this regard, we see that the delayed appearances of crests over HUA are consistent with the eastward drift of F-region plasma. The scenario, just described, is essentially that described for the night of ALTAIR measurements (24 July 1979), which is presented in detail in Tsunoda ([2015](#)).

As expected, the HUA $h'F$ vs LT curve also contains two oscillations, but the crests appeared 28 and 21 min after those in the ATI plot. For a station-separation distance of 180 km, the eastward drift speeds would have been 106 and 143 m/s, respectively. These speeds are not unreasonable for zonal, bulk plasma-transport over Peru (Fejer et al. [1981](#)). If we assume that the bottom edge of the radar backscatter is collocated with the bottomside F layer, we can see that the maximum height difference between JIC and HUA was 180 and 110 km at the times of the first and second crests in the ATI plot. These huge height differences that occurred over a zonal distance of 180 km cannot be associated with the PSSR.

Table 1 Locations of Ionosondes and EAR

| Station	North latitude (°)	East longitude (°)	Dip latitude (°)	ΔLong (°)
Kwajalein (KWA)	9.4	167.5	4.3	–
Pohnpei (PNI)	6.9	158.2	0.6	9.3
Cebu (CEB)	10.3	123.9	2.0	–
Manila (MAN)	14.7	121.1	7.1	2.8
Ho Chi Minh City (HCM)	10.8	106.6	4.0	–
Bac Lieu (BCL)	9.3	105.7	1.6	0.9
Chumphon (CPN)	10.7	99.4	3.3	6.3
EAR Kototabang (KTB)	− 0.2	100.3	− 10.1	− 0.9
Kodaikanal (KOD)	10.2	77.5	1.8	–
Fortaleza (FTL)	− 3.9	− 38.5	− 4.5	− 10.6
São Luís (SLU)	− 2.3	− 44.2	− 0.3	− 5.8
Cachimbo (CCB)	− 9.5	− 54.8	− 2.1	–
Huancayo (HUA)	− 12.0	− 75.3	0.3	–
Jicamarca (JIC)	− 12.0	− 76.9	0.5	1.6
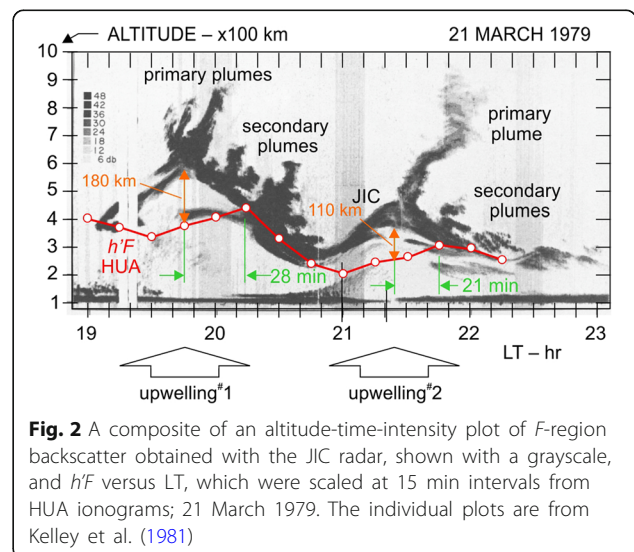
Fig. 2 A composite of an altitude-time-intensity plot of F-region backscatter obtained with the JIC radar, shown with a grayscale, and $h'F$ versus LT, which were scaled at 15 min intervals from HUA ionograms; 21 March 1979. The individual plots are from Kelley et al. ([1981](#))

Velocity and h'F perturbations

Rastogi et al. ([1991](#)) made a direct comparison between V_zF measured every 10 min with the JIC radar and mean vertical velocity ($\Delta h'F/\Delta t$), estimated from the difference between adjacent $h'F$ values; in this case, from HUA ionograms were taken every 15 min. Data were collected from 1968 to 1975 (high to low solar activity). One of his examples, from 16 October 1969, is redrawn in Fig. [3](#). The V_zF values are plotted with red circles (gray fill); the $\Delta h'F/\Delta t$ values are plotted with red circles (white fill). The $h'F$ curve from HUA is plotted below the velocity curves; all are plotted versus LT (at 75°W longitude). This was an active night during high solar activity; there was a strong 'PSSR,' resulting in a high maximum $h'F$ and appearance of strong range spread F (RSF) beyond 2045 LT (vertical line segment), where there is an absence of scaled $h'F$ values. Of interest is the difference in velocities, which appears to vary slowly and coherently for over an hour; the largest difference was 17 m/s, which occurred around 1850 LT during the 'PSSR.' The variations appear to be wavelike and out of phase. If so, the zonal wavelength must have been 360 km (for station separation of 1.6° in longitude), which is similar to a wavelength for LSWS (e.g., Röttger, [1973](#); Tsunoda and White, [1981](#)). Using these estimates, the eastward drift speed must have been close to 130 m/s, which appears reasonable (e.g., Fejer et al. [1981](#)).

Rastogi et al. ([1991](#)) also plotted all data that were available for the times of radar measurements, which include various levels of solar activity. Apparently, $h'F$ values were scaled where possible, which seems to exclude times of strong RSF. We have scaled those points (from their Fig. [2](#)) and replotted them in Fig. [4](#). Blue circles with white fill are their scaled values; we have added red dots, where each represents the average value for the $\Delta h'F/\Delta t$ values, for a plotted V_zF value. (They are collocated with a blue circle, when there is only one $\Delta h'F/\Delta t$ value for that V_zF value.) They performed linear regression on the blue circles to obtain the following:

$$\Delta h^{'}F/\Delta t = 1.4 + 0.67 V_zF \qquad (1)$$

This fitted curve is the thick, sloping gray line in Fig. [4](#). They concluded that the $\Delta h'F/\Delta t$ estimates were essentially 2/3 those of V_zF estimates, and the small bias in the fit was negligible. We can see from the fit to the scatter that Eq. (1) has the best fit for the larger values; we can also see that the clusters are tightest for larger velocity values. We could argue that the larger absolute values were likely associated with high solar activity. And, indeed, similar findings were reported by Fejer et al. ([1989](#)), also
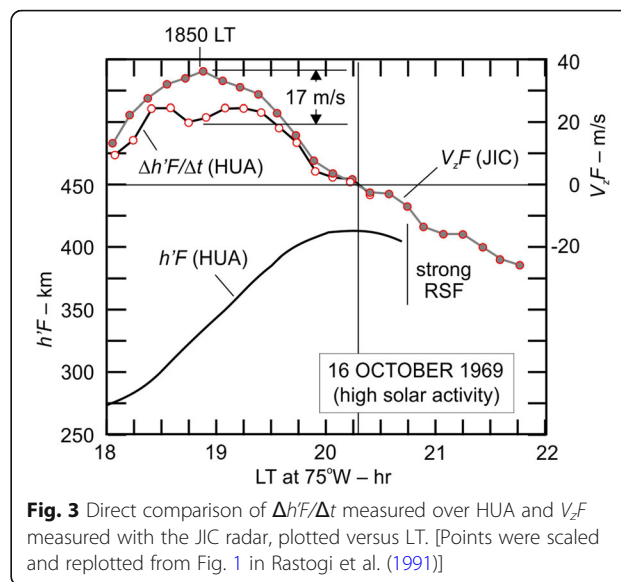

Fig. 3 Direct comparison of $\Delta h'F/\Delta t$ measured over HUA and V_zF measured with the JIC radar, plotted versus LT. [Points were scaled and replotted from Fig. [1](#) in Rastogi et al. ([1991](#))]

for periods of high solar activity; V_zF values were found to be a factor of two larger than $\Delta h'F/\Delta t$ values.

For our purposes here, we are more concerned with uncovering information related to the longitudinal variability in E, and less with the source of the 0.67 scaling factor. But, it may be worth mentioning that a scale factor could arise from an altitude gradient in zonal E (e.g., Sastri et al. [1995](#)); in this regard, the altitudes of V_zF measurements (i.e., near the peak of the F layer) were likely higher than those for $\Delta h'F/\Delta t$ (i.e., closer to the bottomside of the F layer). Our finding, that the tilt angle of the PSSR is steeper at a higher altitude, in Fig. [1](#), is consistent with this notion.

It seems apparent that the scatter in scaled values does not reflect the behavior of a random variable from a single population. Instead, the distribution of scatter suggests presence of processes that may be dependent on velocity. For example, if $\Delta h'F/\Delta t$ measurements truly represent the bulk motion of the F-region plasma, and if they were made simultaneously and in the same location as the V_zF measurements, those pairs of values should all fall on the sloping green line in Fig. [4](#). Interestingly, points that fall between 0 and − 10 m/s do seem to be aligned with the sloping green line, and not with the gray line. It seems that the points with velocities between 10 and 15 m/s also have this alignment, although with larger scatter. And, curiously, the points that fall between 0 and 10 m/s appear to be offset above the sloping green line; this offset in positive values is not mirrored in negative values. Also interesting is the finding that $\Delta h'F/\Delta t > V_zF$ for values between 0 and 10 m/s. As mentioned above, only points with magnitudes greater than 10 to 15 m/s are clearly aligned with the gray line, which is represented by Eq. ([1](#)).
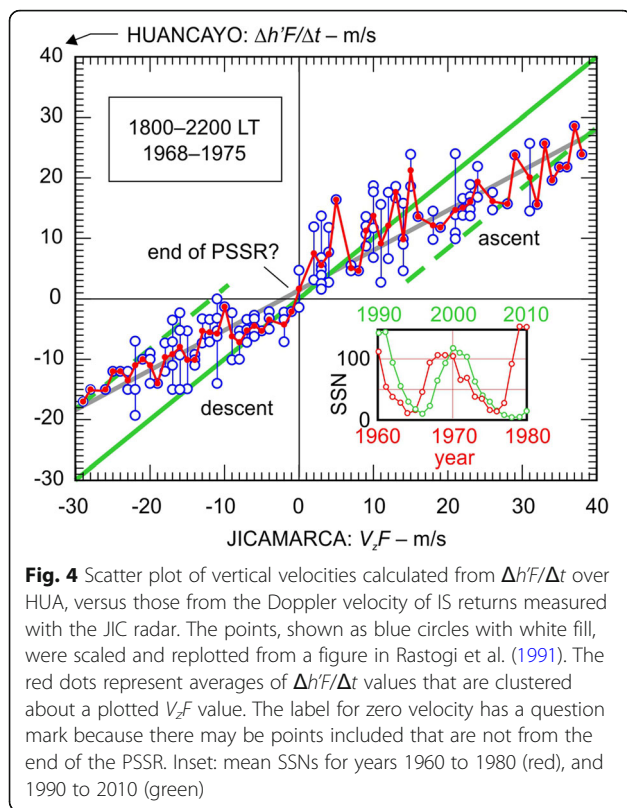
Tsunoda *et al. Progress in Earth and Planetary Science* (2018) 5:22

Page 8 of 28

Fig. 4 Scatter plot of vertical velocities calculated from $\Delta h'F/\Delta t$ over HUA, versus those from the Doppler velocity of IS returns measured with the JIC radar. The points, shown as blue circles with white fill, were scaled and replotted from a figure in Rastogi et al. (1991). The red dots represent averages of $\Delta h'F/\Delta t$ values that are clustered about a plotted V_zF value. The label for zero velocity has a question mark because there may be points included that are not from the end of the PSSR. Inset: mean SSNs for years 1960 to 1980 (red), and 1990 to 2010 (green)

We suggest that the source of the scatter in Fig. 4 has geophysical basis. For example, the findings that velocity reversal was simultaneous (Rastogi et al. 1991) and accompanied by a virtual disappearance of the scatter, could be related to behavior, which occurs near the end of the 'PSSR.' The asymmetry in the tightness of the scatter, near zero, between positive and negative values could be related to upwelling growth during ascent, and even a damping of upwelling modulation during descent. The peak-to-trough span in the scatter is about 10 m/s, which is comparable to the velocity difference of 15 m/s, found on 16 October 1969 (see Fig. 3). Hence, although not recognized at that time, Figs. 3 and 4 support the notion that there can occur significant differences in 'PSSR' at locations (i.e., JIC, HUA) that are separated by only 1.6° in longitude. These results appear to be consistent with the upwelling paradigm ("EPB development: two paradigms").

Low-latitude satellites

Properties of LSWS have been measured with in situ probes on the Atmospheric Explorer *E* (AE-*E*) and San Marco *D* satellites, and a radio beacon (Bernhardt and Siefring, 2006) on the Communication/Navigation Outage Forecasting System (C/NOFS) satellite (de La Beaujardiere et al. 2004). All three flew in low-inclination orbits (see Table 2). In situ measurements consisted of spatial scans

versus longitude in the bottomside of the equatorial *F* layer; TEC measurements, using ground-based radio receivers could be interpreted in terms of altitude-modulated isodensity contours in the bottomside *F* layer.

EPB spawning ground

All three sets of measurements have shown that EPBs develop at longitudes that are occupied by pre-existing upwellings. Singh et al. (1997) presented results from four case studies, all from 1977, a year of low solar activity (see inset, Fig. 4). From consecutive orbits (made at 95 min intervals) that passed over the same longitude sector, they showed that LSWS, with 150 to 800 km zonal wavelengths, preceded the appearance of EPBs and dictated where EPBs would form, as described in the upwelling paradigm. Eccles (2004) reported perturbation *E* (ΔE) measurements made with the San Marco *D* satellite, from 27 August to 4 September 1988 (high solar activity), for the interval between 1600 and 2100 LT. He found that EPBs developed in the post-sunset sector, at longitudes where upwellings were observed during the previous orbit, in the pre-sunset sector. In his case, upwelling regions were associated with an eastward ΔE. This confinement of EPB development to upwelling regions was first demonstrated with ALTAIR (Tsunoda and White, 1981), and have since been demonstrated using TEC measurements obtained with the C/NOFS satellite (e.g., Thampi et al. 2009; Tsunoda et al. 2010, 2011; Tulasi Ram et al. 2012). Additional evidence is presented in the "Case study: 27 March 2006" section of this paper.

Seed LSWS

A key finding is the ubiquitous presence of ΔE in San Marco *D* measurements during the late afternoon and evening (Eccles, 2004). Small-amplitude wavelike perturbation in drift speed of about 5 m/s (scaled from his figures) appeared to be ubiquitous, from as early as 1600 LT, when the solar zenith angle (χ) was 62°. For comparison, SS_E ($\chi \sim 101°$) occurred 2–1/2 h later, around 1839 LT, when the Sun's shadow-height was at 110 km. Observations of LSWS perturbations have also been found in TEC data, using C/NOFS; they include measurements of LSWS, when χ was between 85° and 86.6° (Thampi et al. 2009; Tsunoda et al. 2011, 2013), which occurred before ground sunset. In this regard, it

Table 2 Satellite orbital parameters

Satellite	Inclination (°)	Apogee (km)	Perigee (km)
AE-*E*	19.76	275	275
San Marco *D*	2.9	614	260
C/NOFS	13	850	400

Tsunoda et al. Progress in Earth and Planetary Science (2018) 5:22

Page 9 of 28

is perhaps useful to note that temporal oscillations in virtual height with peak-to-peak amplitudes up to 20 km have been observed (Abdu et al. 2015) within a period band between 0.5 and 1.5 h, using Digisondes at Fortaleza (FTL) and São Luís (SLU). These oscillations were observed from near midday with amplitudes that increased with time toward sunset. If these oscillations are related to the longitudinal variations in ΔE, an implication might be that they are more widespread in occurrence than just the late-afternoon sector, as suggested by the abovementioned satellite measurements.

Given the ubiquity of small-amplitude LSWS and only the occasional development of EPBs, Eccles (2004) concluded that upwellings determine the locations where EPBs appear, but it must be the interchange instability, driven by PSSR, that controls EPB development. In this paper, we show that upwelling growth controls EPB development, and that upwelling growth, itself, may be driven by PSSR and the interchange instability during high solar activity, but not by PSSR during low solar activity (see "Upwelling growth: weak PSSR" section).

Polarization E
Regarding ΔE, Singh et al. (1997) found that ion velocities were upward (downward) inside (outside) of upwellings, with speeds up to 27 (13) m/s. Moreover, horizontal perturbations in zonal U of 10 m/s (peak to peak) were measured that matched perturbations in ion density. The perturbations in ion drift velocity were smaller by a factor of 1.3, which is reasonably consistent with the F-region dynamo (Rishbeth, 1971). Although vertical U measurements were not available, they were likely present, if associated with atmospheric gravity waves (AGWs). All AGWs that propagate upward from the lower atmosphere have a vertical component associated with their downward-tilted phase fronts. The perturbation ion-drift velocities were found to be comparable to those seen in Fig. 4.

Equatorial Atmosphere Radar (EAR) and ionosondes (CPN, KTB)
Results related to LSWS and zonal variability were obtained by using a different set of ground-based instruments, the EAR and two ionosondes, one at CPN and the other at Kototabang (KTB), where EAR is located (Fukao et al. 2006). In this approach, $h'F(2.5)$ curves from ionograms were used to provide information about 'PSSR,' and spatial maps of EPBs from EAR measurements were used to provide the zonal locations of EPBs. More details about the EAR, ionosondes, and the experiment geometry can be found in the "Q3: Was EPB associated with upwelling?" section. Generally speaking, all instruments are, more or less, in the same magnetic

meridian (see Table 1 and right panel in Fig. 14). For this study, they selected datasets from 17 nights in March 2004. Backscatter plumes [which are collocated with EPBs (Tsunoda, 1980)] were seen on 12 nights and not on 5 nights.
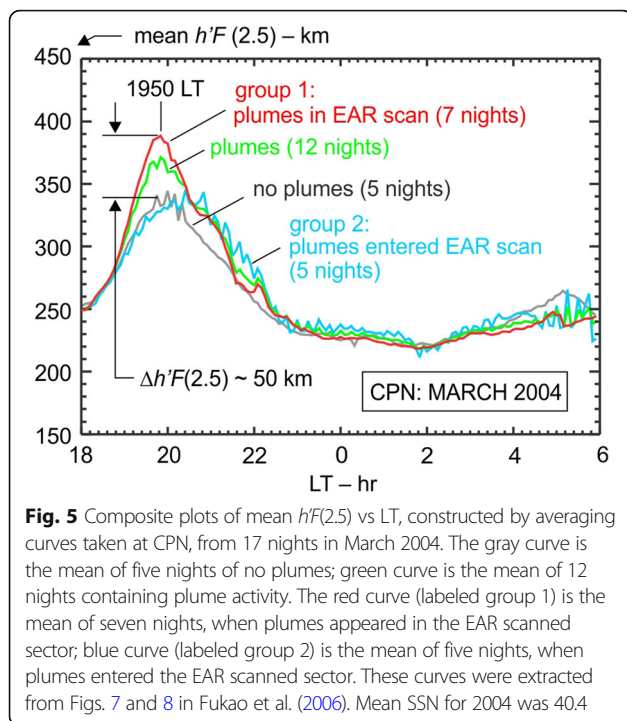
As an estimate for the virtual height of the bottomside F layer, they scaled the virtual height at 2.5 MHz [i.e., $h'(2.5)$]. This choice differs slightly from the use of $h'F$ (e.g., Rastogi et al. 1991), which is defined as the lowest $h'(f)$ along the entire F trace in the ionogram. Because of specific intent, we refer hereafter to $h'(2.5)$ as $h'F(2.5)$. The mean $h'F(2.5)$ curves for these two groups (i.e., plume and no-plume nights) are plotted in Fig. 5. The no plume (on a given night) curve is plotted with a gray line, and the plumes (on a given night) curve is plotted with a green line. The maximum in $h'F(2.5)$ is higher for plume nights than for no-plume nights; this behavior, as expected, is consistent with both paradigms (see "EPB development: two paradigms" section).

An important finding was obtained, when they subdivided the 12 nights when plumes were detected, into two smaller groups, (1) those in which EPBs developed within the sector scanned by the EAR (approximately ± 300 km about the magnetic meridian), around the time of apex sunset (Yokoyama et al. 2004), and (2) those in which EPBs developed to the west of the EAR and drifted eastward, and passed over CPN after apex sunset. The mean $h'F(2.5)$ curve for group 1 is plotted in Fig. 5 with a red line, and that for group 2 with a blue line. Fukao et al. (2006) noted that the maximum $h'F(2.5)$ value for group 1 was higher than that for group 2; moreover, the value for group 2 was essentially the same as that for nights when EPBs were not detected at all. They surmised that the maximum $h'F(2.5)$ must be highest at apex sunset, in all locations where an EPB is born. They estimated the spacing of EPBs to vary from 370 to 1000 km and concluded that they were similar in scale with those of LSWS.

Their finding, that the maximum $h'F(2.5)$ value for group 2 is essentially the same as that for no-EPB night is important because it implies that (1) the maximum $h'F(2.5)$ value for group 1 is associated with upwelling presence, and (2) that for group 2 and no-EPB nights is associated with the PSSR. [It is interesting to note that the difference in maximum $h'F(2.5)$ values of 50 km, shown in Fig. 5, is a typical depth of an upwelling (Tsunoda, 2015).] This conclusion is consistent with the 'PSSR' concept, which allows additive growth by the PSSR and upwelling growth.

Ionosonde–pair studies
Two ionosonde-pair studies have been conducted to investigate spatial differences in electrodynamical behavior, which occurred simultaneously at two closely spaced locations. The first study utilized ionograms from Manila

Tsunoda *et al. Progress in Earth and Planetary Science* (2018) 5:22

Page 10 of 28

Fig. 5 Composite plots of mean *h'F*(2.5) vs LT, constructed by averaging curves taken at CPN, from 17 nights in March 2004. The gray curve is the mean of five nights of no plumes; green curve is the mean of 12 nights containing plume activity. The red curve (labeled group 1) is the mean of seven nights, when plumes appeared in the EAR scanned sector; blue curve (labeled group 2) is the mean of five nights, when plumes entered the EAR scanned sector. These curves were extracted from Figs. 7 and 8 in Fukao et al. (2006). Mean SSN for 2004 was 40.4

(MAN) and Cebu (CEB), which are separated by 2.8 ° in longitude (11 min in LST) and 4.4 ° in latitude (Maruyama et al. 2002); the second study utilized ionograms from CPN and BCL, which are separated by 6.3 ° in longitude (25 min in LST) and only 1.4 ° in latitude (Saito and Maruyama, 2007). In a third study (Abdu et al. 2015), ionograms taken on same nights from FTL and SLU were used, but spatial differences, which might have occurred simultaneously, were not considered. As discussed below, while interpretation becomes complex, when stations are also displaced in latitude, valuable information can be extracted with the help of some modeling. (Location information is presented in Table 1.)

MAN-CEB

Maruyama et al. (2002) presented results, which were derived from measurements made on 10 nights, between 2 and 12 March 1998, a period of high solar activity (see inset in Fig. 4). Ionograms, taken with a 5 min cadence, were scaled to obtain values of the virtual height at 2 MHz [i.e., *h'F*(2)], which they plotted as a function of LT (for 120°E longitude). Maruyama et al. (2002) found that these curves, from MAN and CEB, could be classified into three groups: (1) those that varied identically; (2) those that varied in parallel fashion, but with an offset in which *h'F*(2) over CEB was always 20 to 30 km higher than that over MAN; and (3) those that did not track one another. They showed with simple modeling (e.g., Maruyama, 1996) that the behavior of group 1 could be explained in terms of a weak PSSR and weak *U*, while that

of group 2 could be explained in terms of a moderate PSSR with a significant *U*. The offset in height could be produced by a fixed *U*, which moved plasma along *B* with different magnetic inclinations at the two locations. In essence, the curves in groups 1 and 2 can be explained in terms of global-scale drivers (PSSR and *U*).

Examples with group 3 behavior were found on two nights, when (what is presumed to be) strong range spread *F* (RSF) was also observed. The horizontal bars indicate occurrences of RSF (yellow for CEB, green for MAN). Curves with the largest variations in *h'F*(2) were observed on March 9, which are presented in Fig. 6a. The CEB curve (red circles, yellow fill) has been shifted 11 min to earlier time, to align it with the MAN curve (black triangles, green fill) on the LT scale for 120°E longitude. Features of interest are (1) CEB and MAN curves are identical between 1700 and 1800 LT, indicating solar control through recombination chemistry; (2) *h'F*(2) became higher over CEB with time than over MAN, as the *F* layer lifted, and (3) reversal from ascent to descent occurred first over MAN, then over CEB, 75 min later. (The reversal times are marked by the vertical dashed lines.) A similar pattern of behavior occurred on March 3, which can be seen in Fig. 6b. The time between reversals was also 75 min. The maximum difference in *h'F*(2) between CEB and MAN were 110 km on March 9 and 60 km (not labeled) in March 3.

As noted by Maruyama et al. (2002), the non-parallel behavior of curves in group 3 cannot be explained in terms of only vertical transport (over dip equator) because the *F*-region plasma is essentially incompressible in a plane transverse to *B*. That is, differences in *h'F*(2) over CEB and MAN should not change with time. To accommodate observed behavior, they invoked presence of vertical shear in zonal plasma drift (e.g., Kudeki et al. 1981) and combined it with *h'F*(2) measurements from the two stations, to construct a 2D vortex flow pattern (e.g., Tsunoda et al. 1981; Haerendel et al. 1992; Eccles et al. 1999; Kudeki and Bhattacharyya, 1999).

To illustrate, we have superimposed the flow field, constructed by Maruyama et al. (2002) for March 3, onto Fig. 6b. The superimposed sketch is assumed to be drawn on the vertical plane aligned with the dip equator. The dash-dotted curves represent smooth fits to the data curves for CEB and MAN; the MAN curve has been displaced upward, following *B* lines from the latitude of the station to the equator. The wide (white fill) arrows represent estimates of vertical drift velocity from *h'F*(2) measurements, and the blue arrows represent the vector flow velocity, derived by combining the orthogonal components. This sketch appears to agree quite well with that derived by Eccles et al. (1999), using San Marco *D* measurements with an electrodynamic model. That is, the vortices derived by both methods are similar
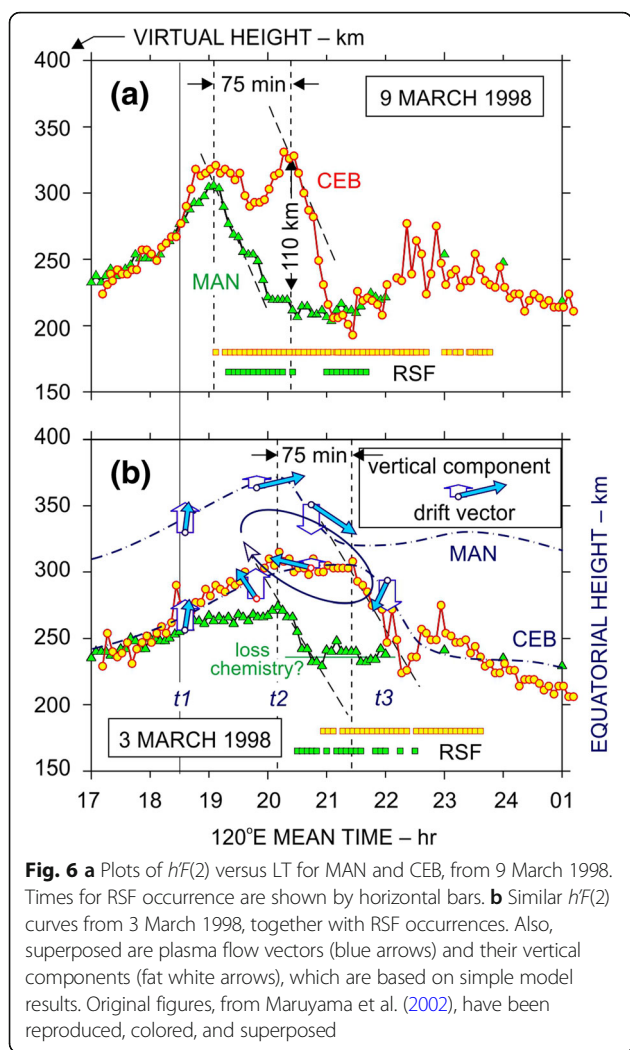
Fig. 6 a Plots of $h'F(2)$ versus LT for MAN and CEB, from 9 March 1998. Times for RSF occurrence are shown by horizontal bars. **b** Similar $h'F(2)$ curves from 3 March 1998, together with RSF occurrences. Also, superposed are plasma flow vectors (blue arrows) and their vertical components (fat white arrows), which are based on simple model results. Original figures, from Maruyama et al. (2002), have been reproduced, colored, and superposed

in that they both extend over a few hours and are centered close to 2030 LT. These results seem to indicate that the simpler pattern of behavior observed in March 3 could be explained in terms of a PSSR that could be a western portion of this equatorial vortex. [We note, however, that there are at least two descriptions that can give rise to a vortical flow (i.e., Eccles et al. 2015; Richmond et al. 2015), and no attempt is made here to evaluate the validity of either description.]

Referring back to Fig. 6a, the double-humped variation in the CEB curve is not unlike the double-humped modulation seen in the HUA curve in Fig. 3. If we assume the peak separation in Fig. 6a to be the station separation of 2.8° in longitude, we obtain a wavelength of 310 km, which is comparable to the 360 km estimate for Fig. 3, and a zonal drift speed of 70 m/s, which is not unreasonable (e.g., Fejer et al. 1981). We could also argue that the curves from Fig. 6a can be envisioned as containing the effects of both the equatorial vortex, as sketched in Fig. 6b, and a superposed LSWS, which would be the double-humped

feature in Fig. 6a. We can further argue that the LSWS, observed over CEB at mean altitude of say, 310 km, may not have mapped up to MAN, which would explain its absence in the MAN curve.

CPN-BCL

The first comprehensive results were obtained with a pair of ionosondes, spaced 6.3° in longitude (Saito and Maruyama, 2007). Using ionograms, taken at CPN and BCL, from March to April 2006, they plotted the $h'F(2.5)$ versus LT curves for CPN and BCL, and found that the curves were similar on nights of no ESF, but substantially different on nights of strong ESF. To illustrate this scatter, they plotted $h'F(2.5)$ values obtained over CPN versus those obtained over BCL, at the same LT, for 12 disturbed nights between March and April 2006 [see their Fig. 3b]. They interpreted $h'F(2.5)$ variations in terms of eastward E variations and concluded that E variations must be localized in longitude, on nights, when ESF occurred. They also used the large difference in zonal scale size between PSSR and ionosonde separation distance to conclude that the variations in $h'F(2.5)$ were likely associated with LSWS, and that their observations were consistent with the 'PSSR' concept, suggested by Tsunoda (2005).

For a closer look at the scatter, which occurred on the most disturbed nights, we selected six nights from their dataset and replotted the $h'F(2.5)$ values in Fig. 7. We note that the plotted pairs of $h'F(2.5)$ values are for the same UT, and not the same LT, as plotted by Saito and Maruyama (2007) in their Fig. 3. We also connected adjacent points and have drawn small arrows next to the curves, so that we can track the direction of transport with time. The points are color coded to distinguish between patterns from different nights. Each set is labeled by the initial letter for the month (M = March, A = April) and by the number for day of month.

Some basic information can be inferred from these curves. The tight clustering of $h'F(2.5)$ values close to 280 km suggests that the 'PSSR' process begins around this altitude; the times are likely close to SS_E. The large scatter of points at lower altitudes is likely associated with times associated with the descent of the F layer. We can use the sloping gray line as a reference, as follows. That is, if the base of the F layer was horizontally stratified and transported vertically, in unison, the $h'F(2.5)$ values would lie along the gray line. But, the PSSR is locked to the solar terminator, which means onset of PSSR would occur later in LST at longitudes farther to the west. In the simplest example, we envision steady upward transport, once the PSSR commences at a given location in longitude. Hence, the base of the F layer would be higher at longitudes to the east, and lower to the west, which should produce a spatial tilt in isodensity

contours (e.g., Fig. 1). This means that $h'F$(2.5) points plotted in Fig. 7 should be below the sloping gray line. In this regard, the M17 (green) curve appears to have behaved, more or less as expected, up to $h'F$(2.5) values over BCL of perhaps 320 km. On the other hand, the A3 (orange) curve appears to have a slope that is opposite in behavior to that expected from the PSSR; it must be indicating presence of sources other than PSSR. The points that deviate farthest from the gray line are those which are likely associated with nights of strong upwelling growth.

Ionosondes (PNI, KWA) and C/NOFS

With the availability of radio beacon signals from C/NOFS, a low-inclination-orbiting satellite (see "Low-latitude satellites" section), it became feasible to gather more comprehensive information about PSSR and upwelling growth, by deploying a cluster of ground-based radio receivers and measuring the TEC variations along several longitudinal tracks. The latter could be interpreted as high-resolution spatial scans of LSWS (e.g., Thampi et al. 2009; Tsunoda et al. 2010, 2011; Tulasi Ram et al. 2012). As before, 'PSSR' information could be extracted from ionosonde-pair measurements.

Tsunoda et al. (2010) conducted a case study, using data collected on 12 September 2009 (solar minimum). Measurements were made with ionosondes at PNI and KWA (9.3° longitudinal separation), and with radio receivers at PNI, KOS, and MAJ. Ionograms from PNI showed that 'PSSR' was essentially zero on this night, while ionograms from KWA showed that 'PSSR' was

weak but not zero. Using scaling arguments ("'PSSR' = PSSR + upwelling growth"), they concluded that PSSR must have been zero over both PNI and KWA, and that the positive 'PSSR' measured over KWA indicated presence of upwelling growth over KWA, but not over PNI. Upwelling growth over KWA was accompanied by strong RSF. From this finding, Tsunoda et al. (2010) concluded that PSSR does not appear to be needed to produce upwellings or RSF, at least not under solar minimum conditions. Further insight can be gleaned by examining the TEC results obtained from measurements made during the first C/NOFS pass (around 0920 UT), which are presented in Fig. 8. Panels (a), (b), and (c) contain plots of vertical (apparent) TEC (i.e., VTEC) versus east longitude for the ionospheric penetration points (IPPs) for PNI, KOS, and MAJ, respectively. The residual VTEC (i.e., δVTEC) is also plotted, which was obtained by subtracting the running averages from the VTEC.

We can see from the blue δVTEC curves (in the lower portion of each panel) that LSWS was not present over PNI, but that it was present to the east of 160°E longitude, just to the east of PNI. The transition from no LSWS to LSWS is clearly seen to take place over perhaps 2 to 3 wavelengths of LSWS, or less than 8 ° in longitude. The longitudinal extent of the LSWS was perhaps as much as 20° in longitude. Hence, we can say that, on this night, PSSR was virtually zero over at least both PNI and KWA, and that upwellings did not develop over PNI, but they did develop, starting just to the east of PNI. Although not shown here, upwelling growth did take place, as can be seen by comparing the results from the first C/NOFS pass (Fig. 8) with a similar plot for the second C/NOFS pass around 1100 UT [see Tsunoda et al. (2010), their Fig. 3]. Hence, a cluster of upwellings can develop in a region that is confined in longitude, as well as perhaps not developing in remaining longitude sectors. More-over, we seem to have evidence that upwelling growth can take place in the absence of a PSSR. Further substantiating results have been obtained from our case study, which is presented in the "Case study: 27 March 2006" section.

Three ionosondes and TEP experiment

A longitudinal chain of three ionosondes (BCL, CEB, GUM) located within a region that is covered by a trans-equatorial propagation (TEP) experiment have provided information about upwelling growth from a different perspective. A TEP experiment is particularly well suited for this task because it provides wide-area coverage with good longitudinal resolution, and measurements can be made continuously in time (e.g., Röttger, 1973). More recently, results have been obtained with a TEP experiment, in which radio transmissions from Shepparton (SHP), Australia, are received at Oarai (ORI), Japan
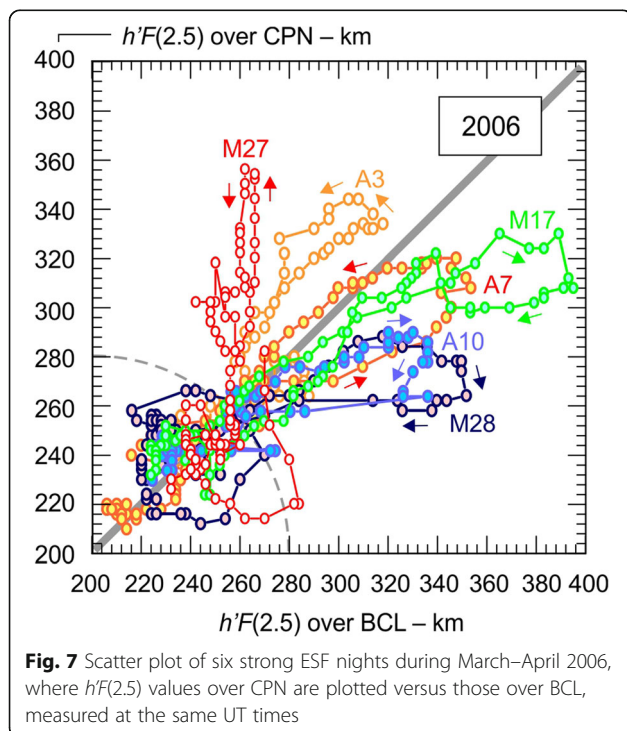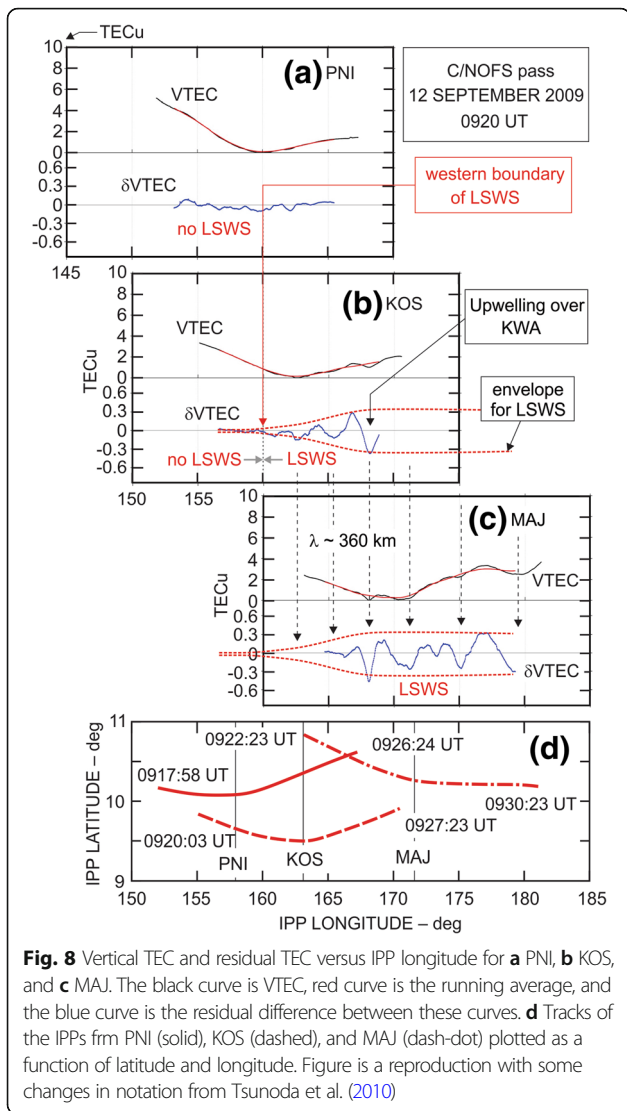

Fig. 7 Scatter plot of six strong ESF nights during March–April 2006, where *h'F*(2.5) values over CPN are plotted versus those over BCL, measured at the same UT times
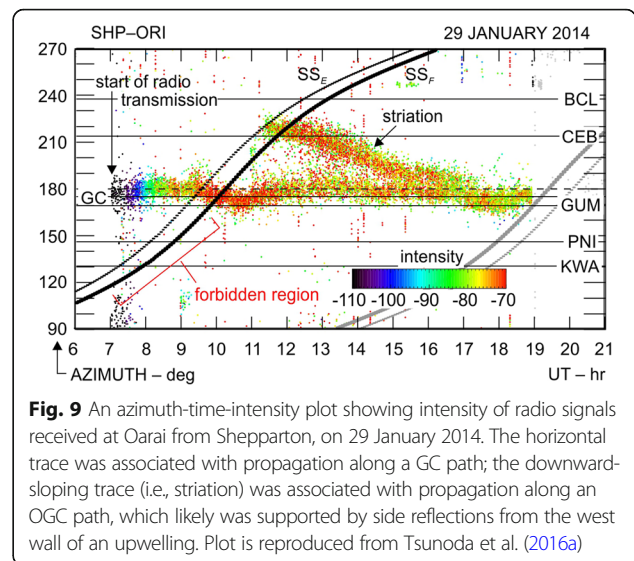
Tsunoda *et al. Progress in Earth and Planetary Science* (2018) 5:22

Page 13 of 28

Fig. 8 Vertical TEC and residual TEC versus IPP longitude for **a** PNI, **b** KOS, and **c** MAJ. The black curve is VTEC, red curve is the running average, and the blue curve is the residual difference between these curves. **d** Tracks of the IPPs frm PNI (solid), KOS (dashed), and MAJ (dash-dot) plotted as a function of latitude and longitude. Figure is a reproduction with some changes in notation from Tsunoda et al. (2010)

(Maruyama and Kawamura, 2006). Examples of two propagation paths that are often supported by this experiment can be seen in the azimuth-time-intensity (AzTI) plot, presented in Fig. 9, reproduced from Tsunoda et al. (2016a). The prominent quasi-horizontal trace, that appears close to 180° azimuth (receive direction) is a great-circle (GC) path, which can be supported by a horizontally stratified *F* layer.

The other, downward-sloping trace, is an off-great-circle (OGC) path, that was likely supported by side reflections from the west wall of an upwelling. This feature, which we refer to as a striation, first appears usually between SS_E and SS_B from a direction between BCL and Cebu (CEB), and then proceeds to drift east-ward with time, which is why it has a downward-sloping appearance. Tsunoda et al. (2016a) showed that an upwelling, detected in ionograms taken at CEB, was indeed associated with this striation.

The finding that an upwelling with sufficient modulation to support an OGC path appeared, starting between SS_E and SS_B and persisted for 5 h, is consistent with all of the results in the "Low-latitude satellites" section through "Ionosondes (PNI, KWA) and C/NOFS" section, as well as those in the "Case study: 27 March 2006" section. Some-what unexpected is the finding that only a single striation was seen on this night. Perusal of other TEP data has shown that observations of multiple striations are rela-tively rare, which suggests that all upwellings in an LSWS (e.g., those in Fig. 8) do not become modulated deeply enough to support OGC paths with long persistence.

Case study: 27 March 2006
Overview
This case study was undertaken as part of a search to find an explanation for some surprising results, which were mentioned in Saito and Maruyama (2007). That is, they found, from ionograms taken with a pair of spaced ionosondes, that *h'F*(2.5) values measured over CPN increased monotonically for 70 min, while those measured over BCL did not. This difference in upward transport, seen in the M27 curve in Fig. 7, produced a height difference of nearly 100 km at locations separated zonally by only 700 km. Our initial reaction was that this difference could not be produced by the PSSR ("Electrodynamics around sunset"); we also felt, as did Saito and Maruyama (2007), that it could be a signature of upwelling growth ("'PSSR' = PSSR + upwelling growth"). The finding that an upwelling can have a modulation depth of 100 km was noteworthy because it not only approached altitudes that are reached by the PSSR, during high solar activity condtions (e.g., Hoang et al. 2010), this height is high enough to lead to EPB development. We have since found that upwelling depth can easily exceed 100 km, as can be

Fig. 9 An azimuth-time-intensity plot showing intensity of radio signals received at Oarai from Shepparton, on 29 January 2014. The horizontal trace was associated with propagation along a GC path; the downward-sloping trace (i.e., striation) was associated with propagation along an OGC path, which likely was supported by side reflections from the west wall of an upwelling. Plot is reproduced from Tsunoda et al. (2016a)

Tsunoda *et al. Progress in Earth and Planetary Science* (2018) 5:22

Page 14 of 28

seen in Fig. 2, and in examples in Tsunoda (2015). Most surprising, however, was the finding that the observed upwelling growth took place under conditions in which PSSR was apparently weak. The notion that upwelling growth contributes to vertical transport is not new (Tsunoda, 2005, 2015); however, we were unaware of how energetic or how commonplace upwelling growth could be during low solar activity.

The objective of this case study is to demonstrate that the large difference in $h'F(2.5)$ values between CPN and BCL, is, in fact, a signature for upwelling growth. We begin by plotting the $h'F(2.5)$ curves versus time, in Fig. 10, and describing the temporal behavior of the difference between the two stations in the "Nature of $h'F(2.5)$ curves" section. We use the disparity in zonal scales, between PSSR and upwelling growth, as a basis for hypothesizing that we are witnessing strong upwelling growth, not a PSSR, over CPN. For our demonstration, we pose four questions, which we claim, by answering affirmatively, represent evidence that supports the upwelling-growth hypothesis. The questions and answers are presented in the "Q1: Was PSSR behavior as expected?" section through the "Q4: Other EPBs and upwellings?" section. The evidence comes from ionograms, taken at three locations [CPN, BCL, and Kwajalein (KWA)], and from backscatter plume data obtained with the EAR.

A summary of physical features found for the night of M27 is presented in Fig. 10, where we have plotted the $h'F(2.5)$ curves from CPN and BCL, and indicated the times when RSF, upwellings, and EPBs, were detected. According to the magnetic Kp indices, given along the top of Fig. 10, magnetic activity was low during the interval of interest. Solar activity was also low during March 2006, when the monthly mean SSN was 27.4 and the observed 10.7 cm solar flux was 75.5×10^{-22} W^{-2}Hz^{-1}.

Nature of $h'F(2.5)$ curves
Quiet-night behavior
The first step is to provide a baseline for understanding, which would allow us to construct a reasonable interpretation for the $h'F(2.5)$ curves in Fig. 10. For example, we can see that $h'F(2.5)$ values for BCL did not reach altitudes nearly as high as those for CPN, but can we say, by looking at the BCL curve, whether PSSR was non-existent on this night, or not? Toward this end, we have also plotted $h'F(2.5)$ curves for two quiet (no ESF) nights in Fig. 10, from 20 to 22 March 2006. Thick lines are used for $h'F(2.5)$ curves from M27; thin lines (solid and dashed) are used for curves from the quiet nights. For all, red and green lines are used for CPN and BCL curves, respectively, which are plotted versus universal time (UT). The local solar time (LST) scale, shown below the UT scale, should be used with the BCL curves. We have also drawn a replica of each CPN curve, using
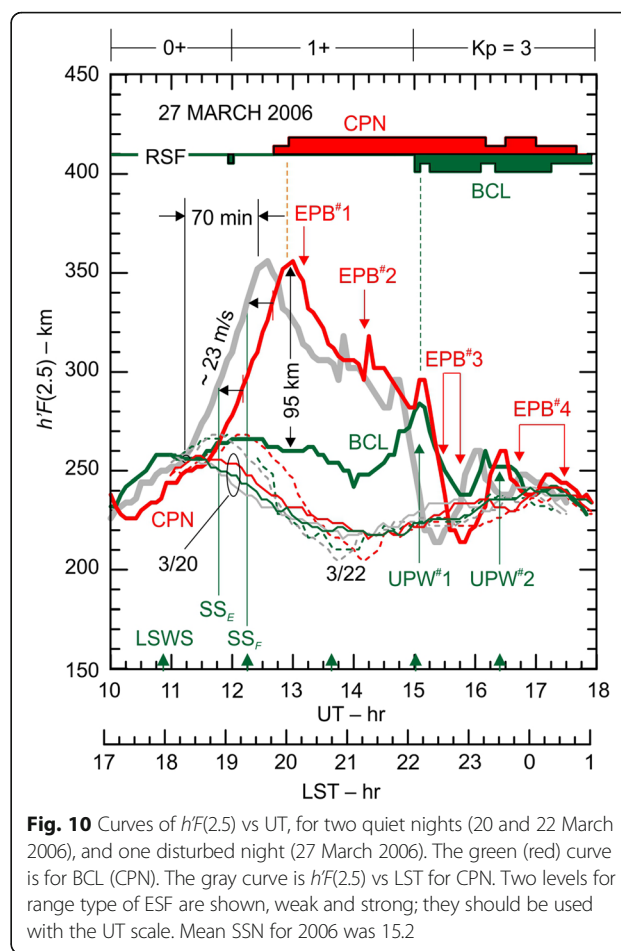

Fig. 10 Curves of $h'F(2.5)$ vs UT, for two quiet nights (20 and 22 March 2006), and one disturbed night (27 March 2006). The green (red) curve is for BCL (CPN). The gray curve is $h'F(2.5)$ vs LST for CPN. Two levels for range type of ESF are shown, weak and strong; they should be used with the UT scale. Mean SSN for 2006 was 15.2

a gray line, which is shifted 25 min toward earlier time. With this displacement, all gray CPN curves can be compared with BCL curves, using the LST scale. For example, the SS$_E$ and SS$_F$ markers can be used with the LST scale for the BCL and gray CPN curves; they can also be used with the BCL (but not CPN) curve to determine their corresponding UT times (i.e., LST at BCL leads UT by 7 h).

Saito and Maruyama (2007) showed that, for no-ESF nights, $h'F(2.5)$ curves from CPN and BCL are similar, when plotted versus LST; this behavior is exactly what would be expected, when bulk vertical transport is solely produced by the PSSR (see "Electrodynamics around sunset" section). That this was the case for the two quiet nights can be seen by comparing the gray and green curves, for a given night, in Fig. 10. If we refer to their scatter plot for 10 no-ESF nights [Saito and Maruyama (2007), their Fig. 3a], we can see that the cluster is tight at $h'F(2.5)$ values below 250 km, but the scatter widens at higher altitudes, which reached 320 km over BCL and 280 km over CPN. The altitude difference can be seen to be as much as 50 km. We can say, however, that $h'F(2.5)$ values did not exceed 320 km on no-ESF nights.

An interpretation could be that, when equatorial F layer is low, its bottomside is horizontally stratified. The source of this stratification could be recombination chemistry, and not necessarily transport effects (e.g., Bittencourt and Abdu, 1981). But, if PSSR is playing a role, vertical transport must occur in presence of a longitudinally extended, eastward E.

As can be seen in Fig. 10, the quiet $h'F(2.5)$ curves from CPN and BCL start tightly clustered around 250 km in altitude, at 1800 LST. Soon thereafter, the March 20 (M20) curves decrease in altitude with time until 2100 LST; the impression is that the PSSR must have been nearly zero on this night. In comparison, the March 22 (M22) curves appear to rise slightly until 1900 LST, before beginning its descent in altitude with time. The descent rate was somewhat more rapid on M22 than on M20, such that they merged near 215 km in altitude, around 2100 LST. Both sets of (green, gray) curves track each other for times after 2100 LST.

Active-night behavior
We now compare the $h'F(2.5)$ curves from M27 with those from quiet nights. Both BCL and gray CPN curves start together with the quiet curves, around 250 km at 1800 LST, which is the expected time for PSSR onset. The BCL curve for M27 appears to rise with time, together with the M22 curve; both become slightly higher than the M20 curve around SS_F. Given that SS_F is around the expected time for the end of PSSR, we can surmise that a weak PSSR occurred on M22 and M27, but not on M20.

Turning to the gray $h'F(2.5)$ curve for CPN in Fig. 10, we see that its behavior is different from the M20, M22, and BCL curves, but it is not unlike the CPN curves in Fig. 5, from March 2004. For example, comparing the CPN curve in Fig. 10 with the red curve in Fig. 5, labeled 'plumes in EAR scan,' we find that their general shapes are similar. Both have narrow peaks, which occurred within 8 min of one another in LST. The maximum $h'F(2.5)$ values were 390 and 355 km for March 2004 and 2006, respectively; their difference may be a solar-activity dependence (e.g., Hoang et al. 2010). These curves, by themselves, are not unusual; each appears to show a rapid PSSR followed by development of strong ESF activity, as expected according to the two paradigms.

We now describe the surprising differences in behavior between the CPN and BCL curves from M27. As noted in Fig. 10, the 'PSSR' rate was 23 m/s over CPN, but only 6 m/s over BCL, which is a difference of nearly a factor of four. [Unfortunately, the estimate for BCL 'PSSR' rate is not accurate because the $h'F(2.5)$ values were below 300 km, where effects of recombination loss chemistry cannot be separated from bulk plasma transport (Bittencourt and Abdu, 1981; Maruyama, 1996).] The

maximum in $h'F(2.5)$ was 355 km over CPN and 260 km over BCL, a difference of 95 km. The behavior of the CPN $h'F(2.5)$ curve, relative to that of the BCL curve, was completely unexpected. That is, given that these measurements are from stations separated in zonal distance by only 6.3° in longitude, both could not be associated with the PSSR of the equatorial F layer.

Quasi-periodic modulation
A feature of interest in Fig. 10 is a wave-like oscillation in the green BCL $h'F(2.5)$ curve between 1700 and 2100 LST. The peak-to-trough modulation was about 10 km. Three crests are discernible with a nominal spacing of 80 min. The first appeared around 1800 LST, well before SS_E, the second appeared close to SS_B and the third appeared during a gradual descent of the $h'F(2.5)$ curve. By plotting the $h'(f)$ curves for integer plasma frequencies, we found that the crest for 2.5 MHz, which appeared at 1315 UT, was in phase with those at 3, 4, 5, and 6 MHz. (The modulation was too shallow to estimate phase accurately for the other two crests, which appeared at earlier times.) It is interesting to see that the gray CPN $h'F(2.5)$ curve also appeared to have a crest around 1800 LST. One interpretation could be that this feature was synchronous with the solar terminator. Another possibility might be that zonal wavelength of this wavelike structure could be the separation distance between CPN and BCL (~ 700 km). We can be sure, however, that the zonal transport speed did not depend on altitude. It is also interesting to find that modulation depth did not increase with time. This behavior would seem to be consistent with the notion that upwelling growth is related to PSSR strength.

This wavelike oscillation appears to be similar to a 'wave-like precursor' observed over Brazil by Abdu et al. (2015). This precursor was seen from local noon to sunset, while growing in amplitude during that period. They found growth to be correlated with PSSR and subsequent development of ESF. Curiously, their oscillations were in phase on all of these active days! Moreover, they found that the peaks for several plasma frequencies were either in phase (as in our case study) or there could be a linear change with altitude, which they suggested might be a signature of AGWs.

There were also two other, larger-amplitude upwellings in the BCL $h'F(2.5)$ curve. Taken together, there were five crests with more or less, equally spaced (see upward-pointing, green arrows along the bottom of the plot). These crests are interesting because they appear to be related to upwellings that either appeared earlier over CPN, or to EPBs that were detected and tracked with the EAR. We have labeled the large-amplitude uplifts as upwellings, UPW[#]1, which appeared around 2200 LST, and UPW[#]2, which appeared around 2330 LST; later, we show ("Q2: Did upwelling arrive over KTB and BCL?"), that UPW[#]1 was likely associated with an upwelling that

Tsunoda *et al. Progress in Earth and Planetary Science* (2018) 5:22

Page 16 of 28

first developed over CPN. We also show ("Q3: Was EPB associated with upwelling?"), that four EPBs developed or passed over EAR and CPN; the times of their passage over CPN are labeled as EPB#1 through EPB#4, in Fig. 10. Although the times of the EPBs are not exact, they are more or less aligned with the green arrows along the bottom of the panel.

Q1: Was PSSR behavior as expected?

To provide an explanation for our unexpected discovery ("Nature of $h'F(2.5)$ curves"), we hypothesize that the large difference in the $h'F(2.5)$ curves, found in Fig. 10, near SS_B was associated with upwelling growth. To be more certain, we can perform two tests. First, given that upwellings are not likely to be amplified prior to the PSSR, we should expect the bottomside F layer to be horizontally stratified before PSSR onset. And second, given that the PSSR is a global-scale feature, we expect behavior outside of an upwelling to be similar over, say, 30° in longitude. In other words, the 'PSSR' curves, measured at locations between upwellings, should be PSSR curves (see Fig. 5 and the "Equatorial Atmosphere Radar (EAR) and ionosondes (CPN, KTB)" section). We can perform the first test by comparing $h'f$ curves from CPN and BCL, for the time interval leading up to the expected time for the PSSR. And, we can perform the second test by comparing the $h'F$ curve from BCL with that from another no-upwelling location.

Comparison of CPN-BCL $h'f$ curves

For the first test, we have plotted $h'f$ curves (integer values of plasma frequency) for CPN and BCL, in Fig. 11. The CPN curves are drawn with thick lines and BCL curves are drawn with thin lines. The numbers next to the curves are the values for plasma frequency in MHz. Identical colors are used for curves with same plasma frequency. We have also included the $h'F(2.5)$ curves from Fig. 10. We can see that the $h'f$ curves from CPN and BCL are similar for times prior to 1130 UT (~ 1830 LST), which means that the bottomside F layer was horizontally stratified at all plasma frequencies above 3 MHz, prior to SS_E. This is expected behavior for locations separated by only 6.3° in longitude. The downward sloping traces, for frequencies as low as 4 MHz, were likely produced by a decrease in underlying ionization as a function of solar zenith angle. The positive slopes found in the 2.5 and 3 MHz curves are likely produced by recombination loss along the bottomside of the F layer, as the solar ionization rate decreased. Hence, ionospheric conditions were, in fact, essentially identical over CPN and BCL at times prior to the PSSR. For times after 1130 UT, the CPN $h'f$ curves indicate upward movement and departure from BCL $h'f$ curves.

For the second test, we have plotted the $h'F(3)$ curve for KWA in Fig. 11, using a thick, chartreuse curve. The

separation distance from BCL to KWA is 61.8 ° in longitude, with a difference in LST of slightly more than 4 h. [Ionograms from Cebu (Table 1) were not available for the time interval of interest.] Although the separation distance is larger than ideal, we include the KWA $h'f(3)$ curve to show that it is similar to that of the BCL curve, up to about 1200 UT (at BCL). Thereafter, the KWA curve droops downward with time, which is similar in behavior to those for the two quiet nights. Although we cannot claim that behavior was quiet over the entire longitude sector, from BCL to KWA, we can say that the 'PSSR' over KWA appears to resemble that over BCL. Hence, this resemblance is supportive of the notion that the 'PSSR' is similar, when measured in regions that are not occupied by upwellings.

Comparison of CPN-KTB $h'f$ curves

With ionograms also available from KTB, which is the site of the EAR, we can check the latitudinal variation in the bottomside F layer. In this regard, we are interested whether an equatorial ionization anomaly (EIA) formed in the late afternoon or early evening. Presence of a daytime EIA would indicate strong E-region dynamo action, which could alter the ratio of the field-line-integrated Pedersen
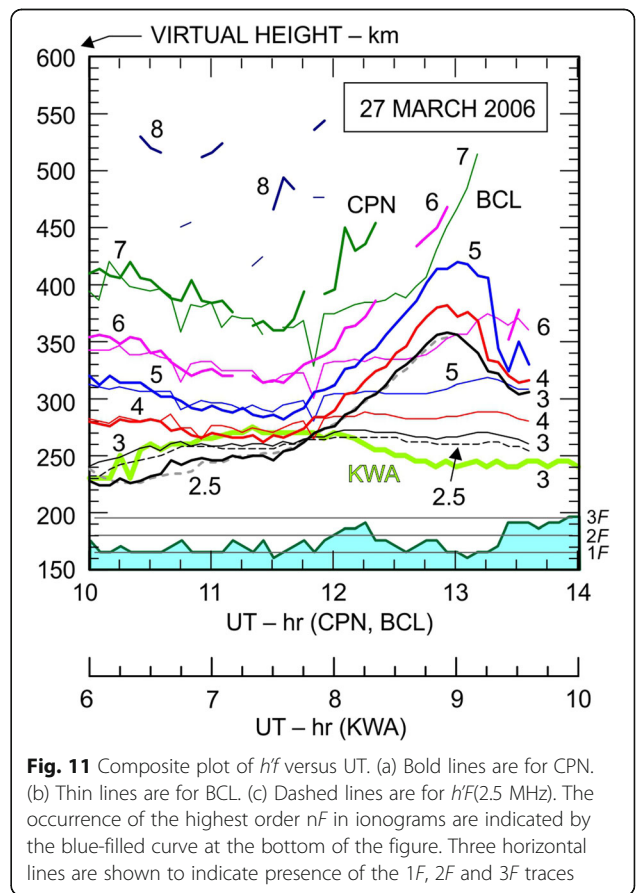

Fig. 11 Composite plot of $h'f$ versus UT. (a) Bold lines are for CPN. (b) Thin lines are for BCL. (c) Dashed lines are for $h'F(2.5$ MHz). The occurrence of the highest order nF in ionograms are indicated by the blue-filled curve at the bottom of the figure. Three horizontal lines are shown to indicate presence of the 1F, 2F and 3F traces

conductivity of the F layer (Σ_P^F) to that of the E layer (Σ_P^E). A higher ratio that persists into the early evening could enhance the vigor of the interchange instability (e.g., Raghavarao et al. 1988; Alex et al. 1989; Sridharan et al. 1994; Jayachandran et al. 1997; Dabas et al. 2003; Thampi et al. 2006, 2008; Prakash et al. 2009; Uemoto et al. 2010). And, the appearance of an evening enhancement would, itself, be an indicator of strong PSSR occurrence. [Note: although this behavior should be associated with high solar activity, we examine its possible presence because there is evidence of its occurrence during low solar activity (Sastri, 1998). See the "Our case study: extreme event?" section]

The $h'f$ curves, using thin lines for CPN and thick lines for KTB, are plotted versus UT in Fig. 12. As in Fig. 11, curves for integer plasma frequencies are plotted, using the same colors for the same plasma frequency. We can see by comparing curves, from Figs. 11 and 12, that the altitude profiles in the bottomside F layer were similar around 1000 UT, at all three locations (CPN, BCL, KTB) , as expected from presence of a horizontally stratified, sunlit F layer at this time. (Even the 3 MHz contour over KWA was similar around this local solar time.) The CPN curves were slightly higher than those for KTB (except at 3 MHz), which may be indicating that F-region plasma simply moved along B to lower altitudes at higher dip latitudes. In other words, the distribution of N at 1000 UT is consistent with the absence of EIA formation during the day.

The altitude profiles did change, however, during the interval from 1030 to 1200 UT, which was followed by the strong 'PSSR' over CPN. The $h'f$ of the KTB curves appear to rise, reaching a maximum around 1100 UT, while those of the CPN curves appear to descend, reaching a minimum between 1100 and 1130 UT. The descent of CPN $h'f$ curves could have been produced by the chemical decay of the underlying F layer with increasing solar zenith angle. If this is what happened, the KTB $h'f$ curves should also have descended. The rise of the KTB $h'(6 \text{ MHz})$ was most abrupt and noticeable, starting around 1030 UT and reaching a maximum only 30 min later. Examining individual ionograms, we found evidence of unusual behavior, possible associated with off-vertical propagation paths. Without pursuing the cause of this anomaly, which is beyond the scope of this paper, we surmise that it may have been associated with upwelling-related structure, but not with enhancements in PSSR. In this regard, we conclude that EIA-enhanced effects did not play a role in this upwelling-growth event.

Q2: Did upwelling arrive over KTB and BCL?
Delay in arrival over KTB
If upwelling growth was responsible for the large $h'F(2.5)$ values over CPN, shortly after SS_B the upward growth in
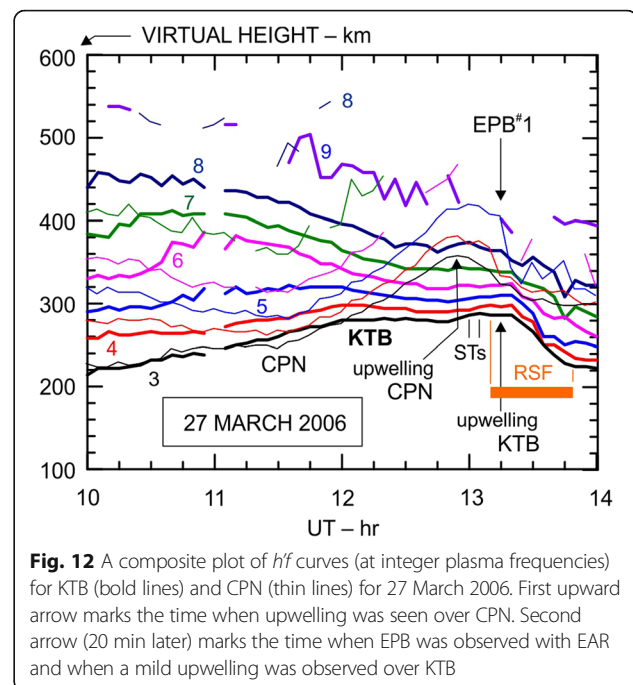

Fig. 12 A composite plot of $h'f$ curves (at integer plasma frequencies) for KTB (bold lines) and CPN (thin lines) for 27 March 2006. First upward arrow marks the time when upwelling was seen over CPN. Second arrow (20 min later) marks the time when EPB was observed with EAR and when a mild upwelling was observed over KTB

altitude over the magnetic equator should have been accompanied by an upward and outward growth (transverse to B), from near the magnetic equator to higher dip latitudes into both hemispheres, as described in the "Ionosonde–pair studies" section and the upward displacement of the MAN curve in Fig. 6b. This occurs because the polarization E (associated with upwelling) maps along B, as it does for an EPB (e.g., Tsunoda et al. 1982). Given the height reached over the dip equator, the upwelling should have arrived over KTB, and its arrival might be expected to produce ionogram signatures, not unlike those found in equatorial ionograms (Abdu et al. 1981; Tsunoda, 2008, 2009). In this scenario, the telling feature would be a delay in appearance of the upwelling over KTB, relative to its appearance over CPN.

Referring back to Fig. 12, we have marked the mean time of appearance of the upwelling over CPN with a labeled arrow. Turning to the KTB curves, there is, indeed, a milder and broader (in UT) uplift, which is centered around 1315 UT (marked with an upward-pointing arrow). The delay in arrival of the upwelling over KTB is about 20 min, relative to its appearance over CPN. In comparison, if the bulk upward transport velocity produced a large-scale E, which was independent of altitude over the dip equator (e.g., Woodman, 1970), the outward transport velocity should occur around the same time at nearby latitudes. In other words, an uplift associated with the PSSR should be detected nearly simultaneously over CPN and KTB. Hence, the delayed appearance of the mild bump in the KTB curve can be considered as evidence in support of upwelling growth.

Tsunoda *et al. Progress in Earth and Planetary Science* (2018) 5:22

Page 18 of 28

Other clues that this feature was produced by the arrival of the upwelling over KTB are the presence of ionogram signatures (e.g., Tsunoda, 2008, 2009; Thampi et al. 2012), which were observed, as indicated in Fig. 12. For example, the two short vertical lines indicate times when satellite traces (STs) were detected, just prior to the arrival of the upwelling. Near the dip equator, STs have been shown to be oblique echoes from tilted isodensity surfaces, such as those associated with the walls of an upwelling. The STs were followed by range spread F (RSF), whose time of presence is indicated by the orange horizontal bar. We see that RSF appeared around the time when the upwelling crest arrived over KTB, and it continued until the upwelling had passed. This association of RSF with the trailing portion of the upwelling is consistent with RSF occurring along the west wall of an upwelling (Tsunoda, 1981, 1983, 2005). The presence of RSF over KTB is also consistent with the onset of RSF over CPN, at the time of upwelling appearance. The implication is that the upwelling extended north-south along the bottomside of the F layer into both hemispheres (e.g., Weber et al. 1978, 1996) and drifted eastward with time, not unlike the behavior of the striation in Fig. 9 (Tsunoda et al. 2016a).

Delay in arrival over BCL
Besides upward and outward growth of an upwelling, which should lead to its slightly delayed appearance over KTB, as discussed above, the same upwelling should have drifted eastward from CPN and arrived over BCL sometime later. Saito and Maruyama (2007) examined this event and estimated that the upwelling in the BCL curve, seen around 1500 UT, and labeled UPW#1 in Fig. 10 ("Nature of $h'F(2.5)$ curves"), is consistent with the arrival of the upwelling, which we hypothesized to have developed over CPN around 1300 UT. If we use 130 min for the time between the peaks, and 700 km as the distance between stations, we obtain a zonal drift speed of 90 m/s, which is close to the 80 m/s drift speed that we estimated from EPB measurements with EAR(see "Q3: Was EPB associated with upwelling?" section).

That an upwelling drifts eastward is expected (e.g., Tsunoda, 2015), but whether it can persist for more than 2 h, the time needed to transport the upwelling from CPN to BCL might be questioned. There is, in fact, substantial evidence that upwellings are north-south-aligned structures that persist for several hours (e.g., Weber et al. 1978, 1996; Tsunoda and White, 1981; Tsunoda, 2015). More recently, Tsunoda et al. (2016a, b) showed that a striation (i.e., a discrete OGC path in a TEP experiment) can, indeed, persist for more than 5 h, as can be seen from Fig. 9 (see "Three ionosondes and TEP experiment" section). If we use 75 (100) min as the duration of the upwelling in the BCL curve, we obtain an upwelling width of 360 (480) km for a drift speed of 80 m/s; this width is typical for upwellings, close to

400 km. Hence, the findings that upwellings did arrive over KTB and BCL, with the expected delays relative to the appearance of the upwelling over CPN, are strong evidence, in supports our hypothesis, that upwelling growth was responsible for the difference in $h'F(2.5)$ values over CPN and BCL.

We note that the onsets of RSF, around the times of appearance of presumably the same upwelling, over CPN, KTB, and BCL, clearly strengthen the evidence in support of this hypothesis. Also, if we can interpret UPW#1 over BCL as the arrival of the upwelling over CPN around SS_B we should be able to interpret the second upwelling over BCL, labeled UPW#2, in terms of an upwelling that must have passed over CPN after SS_F. Looking at the gray CPN curve, there does appear to be a mild 'bump' around 1340 UT, which could be that upwelling. Hence, we can further conclude that both pairs of upwellings were eastward-drifting features that appeared first over CPN then over BCL.

Q3: Was EPB associated with upwelling?
We can strengthen our case for upwellings that drift from CPN to BCL by noting that (1) EPBs should develop from upwellings (Tsunoda and White, 1981; Tsunoda, 2015), and (2) radar backscatter 'plumes' should be collocated with EPBs (Tsunoda, 1980). Given this behavior, which is predicted by the upwelling paradigm, we should be able to compare occurrences and locations of EPBs with those of upwellings, by using the EAR, a 47 MHz phased-array radar, which can map the spatial distribution of plumes (e.g., Fukao et al. 2003; Otsuka et al. 2004; Saito et al. 2008). Before proceeding with comparisons, we first describe the expected relationships among upwellings, EPBs, and plumes that are detectable with EAR, which are sketched in Fig. 13. We assume a curved Earth and the dip equator is shown with a purple line that is aligned with the local vertical direction. The location of EAR is labeled, and the red line shows the direction the EAR must be pointed to be perpendicular to B lines, which are shown with black curves. In addition, we have sketched an N profile with a purple curve; its base is located between 250 and 300 km in altitude.

First, if an upwelling appears in the magnetic meridian plane of EAR, with a crest altitude of 300 km (dotted green curve), it would not be detected with the EAR. The reason is that the localized E, which produced the upwelling, would map along B (curved red line) down to 100 km altitude in the vicinity of EAR. Even an E, which appeared near a peak crest altitude of 355 km would map to an altitude below the base of the F layer. Given that the background N would be low in both the E and the valley region after SS_E, we would not expect radar backscatter from those regions. Hence, the EAR should

Tsunoda *et al. Progress in Earth and Planetary Science* (2018) 5:22

Page 19 of 28

be insensitive to the appearance of an upwelling near the dip equator.

But, it is possible to use EAR detections of EPBs as indicators for the presence of upwellings below the EPBs. That is, according to the upwelling paradigm (Tsunoda, 2015), a primary EPB is launched from the crest of each upwelling. For our purposes here, it is important to mention that there is a 'blind spot,' where backscatter would not be detected by EAR, even in the presence of an EPB. Referring back to Fig. 13, we can see that backscatter associated with an EPB can be detected for altitudes above 450 km over the dip equator, if we assume that the base of the *F* layer is at 250 km everywhere.

We now proceed to examine the EAR data from this night. Measurements, made using eight radar beams, were used to construct the plot shown in the left panel of Fig. 14. Here, SNR (color scale) is for *B*-perpendicular backscatter, which occurred from an altitude of 250 km, which is equivalent to an altitude just below 500 km over the dip equator. SNR is plotted as a function of distance east of the EAR and UT. We will refer to this plot as the longitude-time-intensity (LTI) plot. Using the dashed red arrows as guides, we see that the first echoes (labeled EPB[#]1) were observed around 1310 UT, 100 km to the west of the EAR. We estimated the eastward drift velocity to be 80 m/s for this feature.

The appearance of EAR backscatter, around 1310 UT, seems to be a bit late, given that the peak in $h'F(2.5)$ over CPN was closer to 1300 UT. We can attribute this discrepancy to the 'blind spot' in the field of view, discussed above. That is, we hypothesize that a primary EPB was launched from the crest of an upwelling, which reached the observed maximum $h'F(2.5)$ value of 350 km
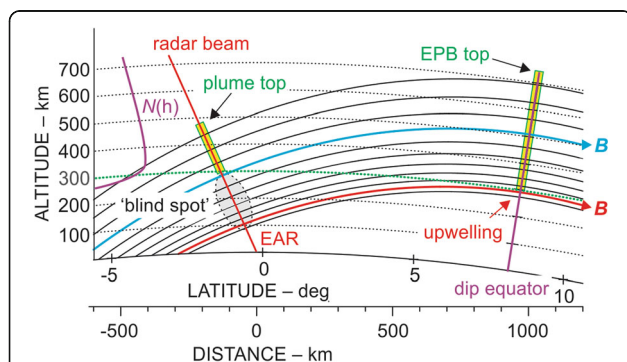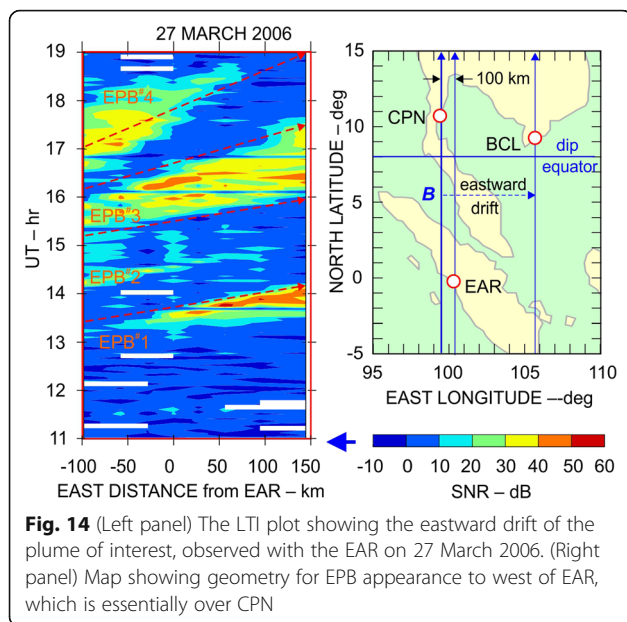

Fig. 13 Sketch of the geometric relationship (in the magnetic meridian) that determines where a plume (green-lined bar with yellow fill) would be detectable with the EAR. The 'blind spot' is a region, below the base of the local *N* profile, where *N* is too low to support radar backscatter, regardless of whether an EPB is present on those *B* lines over the dip equator (which is also shown with a green-lined bar with yellow fill). In other words, plumes can be detected only at altitudes above the blue *B* curve

over CPN. This EPB would not be detected with the EAR until it reached an altitude of 450 km. From Fig. 14, radar backscatter associated with that EPB was not seen until 1310 UT. Noting that $h'F(2.5)$ reached its maximum value around 1300 UT over CPN, we estimate that the EPB grew 100 km in 10 min, which would be an equivalent EPB rise velocity of 167 m/s. Although a bit small, it may not be unreasonable for low solar activity conditions, given that EPB rise velocities of 125 to 350 m/s were measured during high solar activity (Tsunoda, 1981). Hence, the EAR observations are consistent with the notion that an EPB was spawned from the crest of the upwelling observed on M27.

We can also refer to the map, shown in the right panel of Fig. 14. The detection of EPB[#]1, 50 to 100 km west of CPN, is consistent with the viewing geometry. The EAR is located 0.9° in longitude to the east of CPN, and magnetic declination in this region is only 0.5°W. This means *B* is more or less aligned with geographic coordinates. Hence, the detection of EPB[#]1 100 km to the west of EAR places the EPB directly in line with the location of the upwelling, if specified by the maximum in $h'F(2.5)$ over CPN. Having shown that there was an EPB over CPN around 1300 UT, we can argue that these results are consistent with the upwelling paradigm; that is, the backscatter plume appears to be associated with a primary EPB, which was launched from the crest of an upwelling.

Referring back to the LTI plot in Fig. 14, we see that there were at least three other echo groups, up to 1900 UT, which followed the appearance of EPB[#]1. The second, thin backscatter region, which we have labeled EPB[#]2, appeared 100 km to the west of EAR, around 1420 UT, and proceeded to drift eastward with time. Referring back to Fig. 10, we can associate it with the mild maximum in the CPN curve, around 1420 UT. This mild upwelling could have drifted to BCL by 1620 UT, when we see the second upwelling in the thick green curve. With this finding, we can now conclude that the UPW[#]2 in Fig. 10 was associated with both the mild upwelling over CPN and EPBs detected with the EAR.

The next cluster of EAR backscatter, which we have labeled EPB[#]3 in Fig. 14, appeared between 1530 and 1600 UT, 100 km to the west of EAR. This echo cluster does not seem to have a counterpart in the $h'F(2.5)$ curve for CPN. The last cluster of echoes, labeled EPB[#]4, also appeared later in time over CPN. The reason for this mismatch likely comes from a decrease in zonal drift speed with time; this can be seen in the increasing slopes of dashed red arrows in Fig. 14. From this comparison between radar and ionosonde observations, we can surmise that the slow decay in $h'F(2.5)$ curve for CPN may be associated with the presence of tilts, which could support oblique reflections that would be longer in range than overhead reflections.

Tsunoda *et al. Progress in Earth and Planetary Science* (2018) 5:22

Page 20 of 28

Fig. 14 (Left panel) The LTI plot showing the eastward drift of the plume of interest, observed with the EAR on 27 March 2006. (Right panel) Map showing geometry for EPB appearance to west of EAR, which is essentially over CPN

Q4: Other EPBs and upwellings?

An interesting upshot of this study is the realization that the strong upwelling event over CPN at 1300 UT could have been situated on the eastern boundary of a large active region, which contained a cluster of perhaps four or more upwellings. Evidence that upwellings occurred in a cluster comes from the backscatter plume measurements with the EAR. And, we can see from the thick chartreuse curve, drawn in Fig. 10, that the PSSR was very weak over BCL, and that upwellings and ESF did not arrive over BCL (from the west) until after 1400 UT. We could also include the observation of small-amplitude LSWS, up to 1400 UT, as evidence that this was a region in which seed LSWS was not amplified.

We have also shown that similar conditions prevailed over KWA, which is located 60° in longitude and 4 h in LST, to the east of BCL. If we assume 100 m/s eastward drift, an upwelling would travel about 13° in longitude, in 4 h. This means that the absence of activity over KWA for 4 h after its PSSR, can be used to say that upwellings did not develop up to 13° in longitude to the west of KWA. But, we cannot say whether upwellings developed, up to nearly 40° in longitude, to the east of BCL.

The abrupt onset of upwellings, starting over CPN, with more to the west, suggests that some kind of boundary between quiet and disturbed regions may have existed. If so, the transition region was less than 700 km. In fact, Tsunoda et al. (2010) found, using the radio beacon on the C/NOFS satellite and beacon receivers distributed in longitude, that LSWS is a bounded region containing upwellings and that the boundary was quite abrupt, that is, comparable to

700 km. Referring to EAR measurements for M27, we found that there were four clusters of EPBs, spaced about an hour apart in LST. Moreover, the EPB, which appeared over CPN around 1300 UT, was the first in this cluster. Hence, it appears that our interpretation of the dataset is likely, and that other upwellings developed to the west of our featured upwelling. Why the lead upwelling was much larger in amplitude than the trailing upwellings is not yet known.

Upwelling growth model

According to the upwelling paradigm, upwelling growth takes place during the PSSR and the process is thought to be the F-region interchange process. The PRE E, which is responsible for the PSSR, also drives an eastward Pedersen current in the bottomside of the equatorial F layer, where ∇N is directed upward. This geometry is unstable, for the following reasons. The appearance of 'seed' upwelling is associated with a local decrease in field-line-integrated Pedersen conductivity (Σ_P^F), and because this current must remain continuous, the decrease in Σ_P^F will cause an eastward-directed polarization E to appear, as sketched in Fig. 15. This E arises from the positive (negative) charges that will accumulate along the west (east) wall of the upwelling. The upwelling is represented by a red isodensity contour, which is locally uplifted over CPN. From Coulomb's law, it should be apparent that E would be strong within the upwelling, and very weak outside the upwelling, especially in locations that are zonally to the east or west of CPN. The flow pattern should be dipolar (sketched with gray lines), when the upwelling amplitude is small, which is expected from the charge distribution. But as modulation depth increases, the walls of the upwelling should begin to approximate plates of a capacitor, in which case, the flow should be upward within the upwelling, and essentially zero outside of the upwelling region.

This simple interpretation is appealing because it can explain why the 'PSSR' can be so strong over CPN, while it can, simultaneously, be very weak over BCL, as sketched in Fig. 15. In contrast, the PRE E that produces the PSSR should be pervasive over much larger, zonal distances ("Electrodynamics around sunset"). We cannot envision a scenario in which the PRE E would not be similar over CPN and BCL. That this is the case, under quiet conditions, was shown by Saito and Maruyama (2007) (see their Fig. 1a). The other attractive feature of this interpretation is that upwelling growth should be unstable, in the presence of an upward ∇N. As the upwelling pushes upward to higher altitudes, the gravitationally driven Pedersen current should increase and the polarization E should become stronger.

Tsunoda *et al. Progress in Earth and Planetary Science* (2018) 5:22

Page 21 of 28

Our case study: extreme event?

Kodaikanal results

Given that the difference in maximum $h'F(2.5)$ values between CPN and BCL was largest on 27 March 2006, among those measured on 31 nights (Saito and Maruyama, 2007), it is important to try to provide a perspective view. For example, how rare are these events? We found that Sastri (1998) had reported occurrences of abnormally large 'PSSR' velocities in ionograms taken at Kodaikanal (KOD). (Table 1.) He examined ionograms from July 1957 to December 1969, which yielded a dataset of 8 days in which there was a conspicuously large postsunset rise of F region height. All eight events were from equinox and northern winter months, and from 1962 to 1966, years of low solar activity. We can see from the inset plot of yearly mean SSN in Fig. 4 that solar activity for his dataset was comparable to that for 2006, the year of our case study. Sastri (1998) referred to his eight examples as 'extreme' events.

Before comparing our results, it is interesting to note that he found consistent geophysical behavior associated with all of his eight events, which he interpreted as preconditions that lead to an enhanced PSSR. That is, he found the equatorial electrojet (EEJ) to be enhanced, between 1300 and 1600 LT, and the peak of the F layer (i.e., $hpF2$) to be higher, and peak N (i.e., $foF2$) to be lower, between 1600 and 1800 LT. That is, a strong EEJ implies presence of a strong eastward E (associated with the E-region dynamo), and this zonal E would drive the 'equatorial fountain effect' and produce the observed F-layer behavior, as described before (e.g., Raghavarao et al. 1988; Sridharan et al. 1994; Jayachandran et al. 1997). Sastri (1998) interpreted this behavior in terms of a higher, zonal U, because of reduced ion drag, and an increase in Σ_P^F / Σ_P^E. The presumed, enhanced acceleration of the zonal U leads to a stronger PSSR. Whether this scenario could be associated with upwelling growth, as
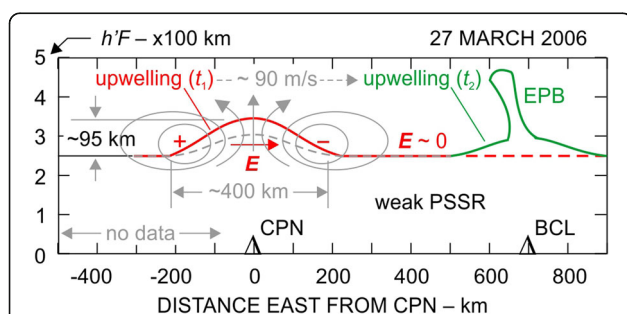
described in the "Case study: 27 March 2006" section, rather than PSSR, remains to be investigated. Interestingly, despite the finding by Sastri (1998) of correlation between extreme events and daytime behavior in EEJ and $hpF2$, there are recent modeling results (Rishmond et al. 2015) that indicate, to the contrary, that the PSSR is more or less independent of daytime electrodynamics.

CPN-BCL results

For comparison with Kodaikanal results, we examined $h'F(2.5)$ curves for CPN and BCL, from 31 nights between March and April 2006. We found six events that could be classified as extreme events, if we define such events as having maxima in $h'F(2.5) > 335$ km. The $h'F(2.5)$ curves that meet this criterion are plotted in Fig. 16a. The curves are labeled with an initial for the month and a number for the day of the month (e.g., M28 = March 28, A10 = April 10). The curves are also labeled with peak altitude and the station initial [e.g., 396(B) = 396 km over BCL]. We have traced one of Sastri's extreme events (14 March 1963) and overlaid it onto Fig. 16a, using a chartreuse line. We can see that it is virtually identical to the BCL curve from 17 March 2006. And, the CPN curve from M27, falls under the envelope formed by the two highest curves. Hence, our extreme events are similar to those in Sastri (1998). From our six cases, we can say the occurrence frequency for extreme events during March–April 2006 was about 19%.

All of the $h'F(2.5)$ curves from the other station (CPN or BCL), for those six nights, are plotted in Fig. 16b. The same color code is used in Figs. 16a, b. If we refer back to Fig. 10 and compare the quiet-night curves with those in Fig. 16b, we find that most of these extreme-event-night curves are generally higher than those from quiet nights. We can use the M27 curve in Fig. 16b and the BCL curve in Fig. 10 as references for this comparison. We note that (1) the BCL (or M27) curve is the lowest of the 'other station' curves for extreme-event nights, which means all of these curves are well above those from quiet nights, and (2) the times when the maximum $h'F(2.5)$ occurred are variable, which should not happen, if associated with the PSSR. From this behavior, we are led to conclude that upwellings are present over both stations, during most, if not all, of these extreme events. This also means that the PSSR was smaller than the observed 'PSSR' most of the time. If this is the case, it becomes difficult to say whether the PSSR was large enough to amplify the upwelling via the interchange instability.

TEP results

Maruyama and Kawamura (2006) tallied and plotted the monthly occurrences of striations, from February 2003 through December 2005 (see their Fig. 10). A principal maximum was found to occur during Spring equinox,

Fig. 15 A sketch showing growth of an upwelling (red curve) over CPN, but not over BCL (red dashed line), at time t_1, and the arrival of the same upwelling over BCL (green line) at time t_2. In this sketch, we show (for simplicity) the absence of a PSSR over both CPN and BCL. The separation between CPN and BCL is 6.3° in longitude and 25.2 min in LST

Tsunoda *et al. Progress in Earth and Planetary Science* (2018) 5:22

Page 22 of 28

and a much weaker, secondary maximum was found to occur during Fall equinox. The number of maximum occurrences was 23 in March 2003, 14 in February and March 2004, and 16 in March 2005. These estimates suggest an occurrence frequency of 50%, or greater, which is higher than that for extreme events in our dataset. One explanation could be that striation occurrences decrease with declining solar activity. The mean SSNs for these years were 63.7, 40.4, and 29.8.; the mean SSN was 15.2 for 2006. It is also possible that their estimates are high, if Maruyama and Kawamura (2006) counted striations of any duration. Noting that the upwelling over CPN on M27 took 2 h to drift to BCL, we suggest that our extreme events are related to deep upwelling events and OGC paths with long persistence.

Fig. 16 a Curves of *h′*(2.5) from six nights, which can be classified as 'extreme' events, observed over CPN or BCL, are plotted with the *h′F* curve for a single 'extreme' event over Kodaikanal (Sastri, 1998). **b** The *h′*(2.5) curves from the other station (over either CPN or BCL. Observations are from March to April 2006

Discussion
Summary of findings

1. Seed upwellings (or LSWS) with zonal dimensions of a few hundred kilometers, appear to be ubiquitous, at least between 1600 and 2100 LT, during high solar activity (Eccles, 2004). Vertical perturbation-drift speeds were found to be about 5 m/s. Because EPBs are not ubiquitous, Eccles (2004) concluded that presence of a seed is not sufficient for EPB development.

2. Perturbation drift speeds can reach 27 (13) m/s inside (outside) upwellings before EPBs develop (Singh et al. 1997). These estimates, measured in situ, are consistent with differences in 'PSSR' rates of 10 to 20 m/s, measured with station separated by 1.6° to 6.3° in longitude (Rastogi et al. 1991; also Fig. 9). These values, which are larger than the ubiquitous residual speeds, indicate upwelling growth.

3. The measured 'PSSR,' is the sum of PSSR and upwelling growth inside an upwelling, and mainly PSSR outside an upwelling (e.g., Tsunoda and White, 1981; Tsunoda, 2005, 2015; Fukao et al. 2006).

4. Upwellings grow, starting around SS_E, and attain modulation depths of 50 to more than 100 km by SS_F (e.g., Tsunoda, 2015; "Case study: 27 March 2006"), which are comparable to altitudes reached during a strong PSSR.

5. Upwellings can have modulation depths comparable to those for strong PSSR, even when the PSSR is very weak [Tsunoda et al. (2010), "Case study: 27 March 2006"].

6. There is mounting evidence that EPBs develop where there are pre-existing upwellings (LSWS) [e.g., Tsunoda and White (1981); Kelley et al. (1981); Singh et al. (1997); Eccles (2004); Fukao et al. (2006); Thampi et al. (2009); Tsunoda et al. (2011, 2016a, 2016b); Tulasi Ram et al. (2012); "Equatorial Atmosphere Radar (EAR) and ionosondes (CPN, KTB)" and "Case study: 27 March 2006," and additional references in Tsunoda (2015)].
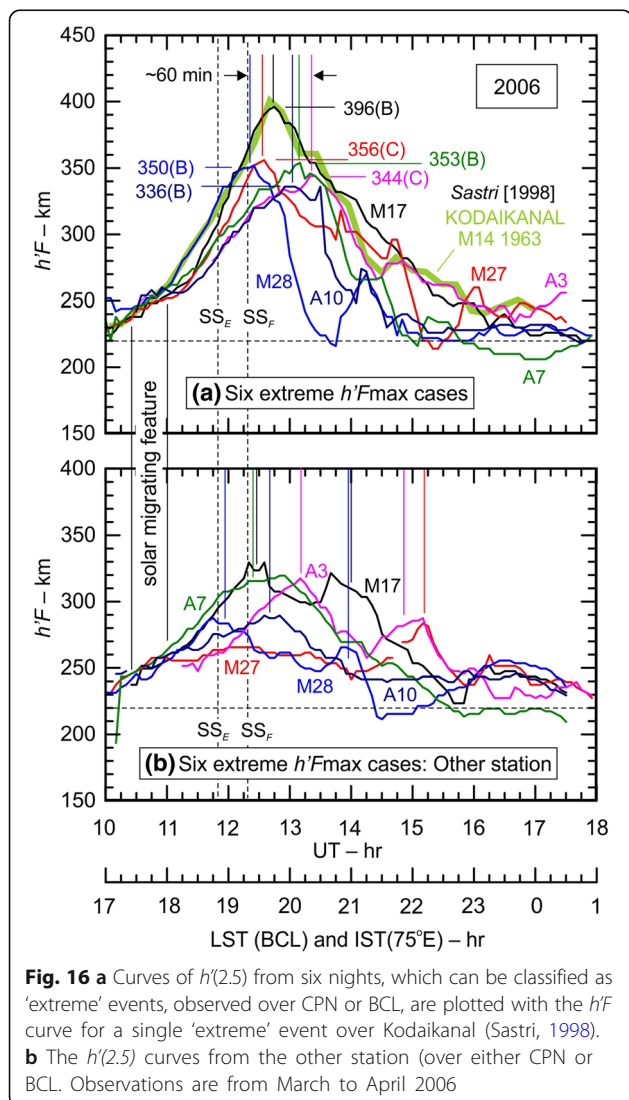
Upwelling growth: weak PSSR

Our breakthrough discovery (finding[#]5), that strong upwelling growth occurs, even when the PSSR is weak (e.g., low solar activity), warrants discussion, if not an explanation. According to the upwelling paradigm (Tsunoda, 2015), upwelling growth is produced by the interchange instability with PSSR as the primary driver (see "Upwelling growth model" section). But if PSSR is weak, we are left without a replacement driver for the interchange instability because other known drivers (gravity, downward U) do not appear to be strong-

Tsunoda *et al. Progress in Earth and Planetary Science* (2018) 5:22

Page 23 of 28

enough contributors, when *F*-layer altitude is low. That is, the gravitational current, proportional to g/ν_{in} (where *g* is gravitational acceleration, ν_{in} is ion-neutral collision frequency), is small because ν_{in} decreases with altitude (e.g., Dungey, 1956; Farley et al. 1970), and downward *U* is expected to be small, when PSSR is weak (Sekar and Raghavarao, 1987; Sekar and Kelley, 1998; Sekar et al. 1994; Raghavarao et al. 1993).

Instead, we could argue that upwelling amplitude actually depends on initial seed-amplitude as well as the growth rate of the interchange instability. So, when growth rate is weak, it is conceivable that seed plasma-perturbation is strong enough to conpensate to preserve strong upwelling growth. One possible scenario that could produce stronger seed-amplitude is described in the next section ("Strength of 'seed' plasma perturbations"). On the other hand, we recall, from finding[#]1 ("Low-latitude satellites"), that the residual LSWS-related perturbation is about 5 m/s (high solar activity), but this amplitude appears inadequate to initiate EPB development (Eccles, 2004). And, from finding[#]2, the LSWS-related *E* in an upwelling, which led to EPB development, was found to be larger, or became larger, than 5 m/s. And, we cannot ignore the fact (from our case study) that an upwelling grew at a rate of 20 m/s for 70 min, while PSSR was weak (finding[#]5).

Is PSSR necessary?

While puzzling over potential scenarios of upwelling growth and EPB development that could function when PSSR is weak, we arrived at an intriguing new possibility: could it be that upwelling growth, and not PSSR, is the central player in EPB development? The line of thinking could proceed as follows. On a D2D basis, we observe 'PSSR' and EPB occurrence. There are four possible combinations: (1) low 'PSSR,' no EPBs; (2) high 'PSSR,' EPBs; (3) high 'PSSR,' no EPBs; and (4) low 'PSSR,' EPBs. The first combination, which we call a quiet night ("Nature of *h'F*(2.5) curves"), does occur (e.g., Saito and Maruyama, 2007), and it can be explained in terms of weak PSSR and no upwelling growth. The second combination is consistent with prediction of the PSSR-to-ESF paradigm (i.e., high PSSR) and with that of the upwelling paradigm (i.e., strong upwelling growth). Notice, here, that high 'PSSR' could imply presence of only strong upwelling growth, which would allow us to conclude that a high PSSR may not be necessary.

The third combination could involve either a high PSSR with no EPBs, or high upwelling growth with no EPBs, or both. In the first case, the growth rate of the interchange instability could be reduced by a meridional *U*, which could produce an asymmetry in the hemispheric distribution of *N* (Maruyama, 1996; Saito and Maruyama, 2006; Maruyama et al. 2008, 2009). To our knowledge, thus far, occurrences of the second case are rare. We can also state that occurrences of the fourth combination are also rare, but they do seem to happen (e.g., Tsunoda et al. 2010).

There is evidence (finding[#]6) that EPBs develop from within the confines of an upwelling, regardless of whether PSSR is weak or strong (Tsunoda, 2015). The corollary is EPBs do not develop in regions outside of an upwelling. Keeping in mind that 'PSSR' ~ PSSR in regions outside of upwellings (finding[#]3), we are led to conclude that EPB development requires upwelling growth and, not necessarily, a strong PSSR.

If EPB development is not dependent of PSSR strength, we should be able to show that EPBs do not develop, even when PSSR is strong, if an upwelling is not present. To demonstrate, we refer back to Fig. 5; the gray curve represents the mean for five nights, when EPBs were not detected with the EAR. If we argue that a no-EPB night implies the absence of upwellings, the gray curve must represent PSSR behavior on those nights. Hence, we are led to conclude that 'PSSR' ~ PSSR, and that maximum *h'F*(2.5) was close to 340 km, which is high for a no-EPB night. On the other hand, we have no information about the meridional *U*.

How about velocity shear?

Observations have shown that, while seed upwellings appear in the late afternoon and become amplified around SS_E, EPBs do not appear during upwelling growth; instead, EPBs begin to appear around SS_F in regions already occupied by upwellings. According to the upwelling paradigm ("EPB development: two paradigms"), this sequence of events could arise because of the presence of a vertical shear in zonal plasma drift (e.g., Kudeki et al. 1981; Tsunoda et al. 1981). This process could act as a low-pass filter, allowing growth of LSWS scales, while suppressing growth of EPB scales (e.g., Guzdar et al. 1982, 1983; Satyanarayana et al. 1984).

The results from Guzdar et al. (1982, 1983), who first considered this possibility, are presented in Fig. 17. To illustrate this effect, they plotted three curves. Curve A represents the normalized growth rate of the Rayeligh-Taylor instability, which is the interchange instability with gravity (*g*) as driver. As expected, the growth rate is maximum for $kL >> 1$, where *k* is the wavenumber and *L* is the gradient scale length for *N*. Curve B represents the normalized growth rate of the collisionless Kelvin-Helmholtz (KH) instability with $g = 0$. For this limit, the growth rate, small but still positive, maximizes at $kL < 1$. For this particular curve, $kL \sim 0.4$, which means that for $L \sim 25$ km (e.g., Tsunoda, 1983), we have a zonal wavelength of about 390 km. According to Fig. 17, this wavelength would decrease somewhat if there is a

contribution from the interchange instability. These rough estimates are consistent with the observed scales for upwellings or LSWS (e.g., R ttger, 1973; Tsunoda and White, 1981; Oya et al. 1982; Singh et al. 1997; Eccles, 2004; Fukao et al. 2006; Makela and Miller, 2008; Makela et al. 2010; Tulasi Ram et al. 2014). Hence, we are led to the possibility that velocity shear could contribute to upwelling growth in the absence of a PSSR.

Strength of 'seed' plasma perturbations

There are several scenarios by which LSWS could be seeded and amplified, but to describe them here is beyond the scope of this paper. Instead, we briefly describe one that is promising. That is, upwelling growth could involve an AGW that propagates upward from below to the base of the F layer, where neutral-ion coupling occurs in the presence of an upward ∇N. An AGW is attractive because it produces a wavelike modulation in the vertical component U. This perturbation in vertical U drives a zonally-alternating Pedersen current, which is divergent. Hence, a polarization E appears to cancel this divergence. This oscillating E produces vertical $E \times B$ plasma transport, but a plasma structure does not form if background N is uniform (e.g., near the peak of the F layer). Hence, plasma perturbations appears only in the bottomside F layer by this neutral-ion coupling process (e.g., Klostermeyer, 1978; Huang and Kelley, 1996a, b; Tsunoda, 2010a, b, c).

Seeding without PSSR

The above-described process is appealing because it can operate without presence of a PSSR. There are, however, details that should be considered. For example, the oscillating U drives an F-region Pedersen current, which can be short-circuited by a highly conducting, solar-produced E layer. In this regard, we often use SS_E as the time of demarcation, after which F-region dynamo effects should prevail. But, a perturbation E was ubiquitous, even as early as 1600 LT, which is well before SS_E (see "Low-latitude satellites" section). Eccles (2004), however, has stated that F-region dynamo effects should prevail as early as 1600 LT, presumably, because $\Sigma_P^F > \Sigma_P^E$ [also, see Crain et al. (1993)]. Given that LSWS forms along the bottomside F layer, it is not obvious, without careful modeling, whether the E- or F-region dynamo is controlling this process. If the E-region dynamo is in control around 1600 LT, there would be need to consider a neutral-ion coupling process, other than the one described above.

Another concern is that the amplitude of LSWS perturbation cannot be estimated so easily, because it depends on a chain of events that occur before the AGW participates in the above-described neutral-ion coupling process. The AGW must be convectively
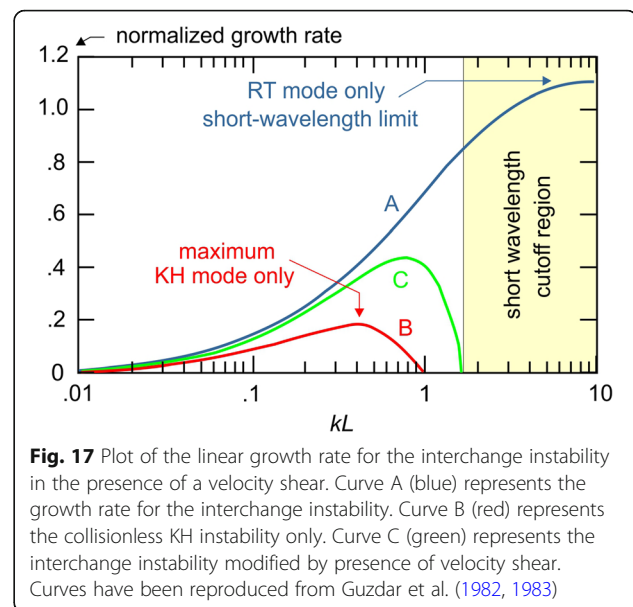

Fig. 17 Plot of the linear growth rate for the interchange instability in the presence of a velocity shear. Curve A (blue) represents the growth rate for the interchange instability. Curve B (red) represents the collisionless KH instability only. Curve C (green) represents the interchange instability modified by presence of velocity shear. Curves have been reproduced from Guzdar et al. (1982, 1983)

generated in the lower atmosphere and propagate up to the base of the F layer. During its upward migration, the AGW undergoes fluid amplification because of decreasing neutral density with altitude, and it may suffer attenuation or reflection, depending on U profile of the background atmosphere. Whether the AGW can couple efficiently with the plasma will depend on its direction of propagation and other wave properties. Hence, we are still far from being able to estimate the LSWS seed amplitude. But, given the host of possible encounters leading up to and including the neutral-ion coupling process, we have good reason to expect variability in upwelling growth properties. Whether any process, or a combination of a few, can produce what we found in our case study, remains to be seen.

Conclusions

We have conducted a comprehensive study on the roles played by upwellings in equatorial electrodynamics and in the development of EPBs. This study was initially motivated by a desire to understand how 'PSSR' could be so strong over one station and so weak over another station, which is separated by only 700 km in zonal distance (Saito and Maruyama, 2007). We found that some sense and order could be attained by assuming that PSSR is a global-scale process and that upwelling growth is a local-scale process. The ratio of scales appears to be an order of magnitude (3000/300). With this assumption, most of the temporal and spatial variability found in various measurements could be attributed to upwelling (LSWS) properties (perhaps superposed on PSSR in the background). We further note that a nominal structure with a zonal spatial scale of 360 km, which drifts eastward with a speed of 100 m/s,

Tsunoda *et al. Progress in Earth and Planetary Science* (2018) 5:22

Page 25 of 28

would be observed to have a temporal scale of an hour. Hence, the temporal variations that appear, for example, in Fig. 16, are likely associated with LSWS. And, indeed, ΔE variations measured by San Marco *D* (Eccles, 2004) contained spatial scales that are well matched to those of LSWS.

We cannot yet say whether the observed wavelengths of LSWS are those of AGWs that arrive in the thermosphere from below (e.g., Vadas, 2007), or whether the local maximum in growth rate of the Kelvin-Helmholtz instability is playing a role because of the presence of velocity shear (e.g., Guzdar et al. 1982, 1983). Another possibility is that wavelength selection is affected by the neutral-ion coupling process, which could include factors such as the degree of alignment between AGW phase fronts and *B* (e.g., Huang and Kelley, 1996b; Tsunoda, 2010b, c) and the interaction time that is available between AGW phase velocity and the zonal plasma drift speed in the bottomside of the equatorial *F* layer (e.g., Whitehead, 1971; Kelley et al. 1981; Tsunoda, 2007). For example, the upwelling growth speed was only about 23 m/s, but growth appeared to persist for 70 min.

The upshot of this study is that the upwelling paradigm, as described by Tsunoda (2007), appears to remain valid for conditions of high solar activity, when PSSR is strong. It still seems reasonable to assume that velocity shear is playing a role in selecting a preferred wavelength for LSWS, while suppressing EPB development up to the time around SS_F. Or, EPBs simply do not appear until upwelling amplitude becomes large enough; and when they do, they strongly prefer the environment within the confines of an upwelling for EPB growth. The main revisions that are needed for the upwelling paradigm are for conditions of low solar activity, when PSSR is weak. We surmise that, enhancements in seed amplitude, in neutral-ion coupling, or in the growth rate of the KH instability, may be able to conpensate for the demise of the interchange instability, as the source for upwelling growth.

Clearly much remains to be done. The key findings from this study point to a need to reconsider the roles that are thought to be played by PSSR and upwelling growth in the development of EPBs. It is important that we recognize that the both PSSR and velocity shear are parts of the vortex that forms in the nighttime equatorial ionosphere, and that the properties of PSSR and velocity shear are likely coupled through vortex electrodynamics. Of interest, for example, is what happens to velocity shear when PSSR weakens? For our revised upwelling paradigm, velocity shear, perhaps together with enhanced seed amplitude, has been suggested as the source for upwelling growth during low solar activity. Whether this notion is correct or not, remains to be determined. In any case, results from this study have at least strengthened the case for the importance of upwellings in EPB development.

Abbreviations

∇*N*: Gradient in *N*; 1D: One dimensional; 2D: Two dimensional; A: April; AE-*E*: Atmospheric Explorer *E*; AGW: Atmospheric gravity wave; ATI: Altitude-time-intensity; AzTI: Azimuth-time-intensity; *B*: Geomagnetic field; BCL: Bac Lieu; C/NOFS: Communications/Navigation Outage Forecasting System; CCB: Cachimbo; CEB: Cebu; CPN: Chumphon; D2D: Day to day; *E*: Electric field; EAR: Equatorial Atmosphere Radar; EPB: Equatorial plasma bubble; EPB#1: Equatorial plasma bubble #1; ESF: Equatorial spread *F*; FTL: Fortaleza; *g*: Gravitational acceleration; GUM: Guam; HUA: Huancayo; IPP: Ionospheric penetration point; IS: Incoherent scatter; JIC: Jicamarca; KOD: Kodaikanal; KTB: Kototabang; KWA: Kwajalein; LST: Local solar time; LSWS: Large-scale wave structure; LT: Local time; LTI: Longitude-time-intensity; M: March; *N*: Plasma density; OGC: Off-great-circle; PNI: Pohnpei; PRE: Pre-reversal enhancement; PSSR: Post-sunset rise; RSF: Range spread *F*; SLU: São Luis; SNR: Signal-to-noise ratio; SS_E: *E*-region sunset; SS_F: *F*-region sunset; SSN: Sunspot number; TEC: Total electron content; TEP: Trans-equatorial propagation; *U*: Neutral wind; UPW#1: Upwelling #1; UT: Universal time; VTEC: Vertical TEC; V_zF: Upward transport velocity; δVTEC: Residual VTEC

Authors' contributions

All authors have read and approved the final manuscript.

Competing interests

The authors declare that they have no competing interests.

Publisher's Note

Springer Nature remains neutral with regard to jurisdictional claims in published maps and institutional affiliations.

Author details

[1]Center for Geospace Studies, SRI International, 333 Ravenswood Ave., Menlo Park, California 94025, USA. [2]Electronic Navigation Research Institute, Tokyo, Japan. [3]National Institute of Information and Communication Technology, Tokyo, Japan. [4]Ho Chi Minh City Institute of Physics, Vietnamese Academy of Science and Technology (VAST), HCMC, Vietnam.

References

Aarons J (1993) The longitudinal morphology of equatorial F-layer irregularities relevant to their occurrence. Space Sci Rev 63:209

Abdu MA, Batista IS, Bittencourt JA (1981) Some characteristics of spread F at the magnetic equatorial station Fortaleza. J Geophys Res 86:6836

Abdu MA, de Medeiros RT, Bittencourt JA, Batista IS (1983) Vertical ionization drift velocities and range type spread F in the evening equatorial ionosphere. J Geophys Res 88:399

Tsunoda *et al. Progress in Earth and Planetary Science* (2018) 5:22

Page 26 of 28

Abdu MA, de Souza JR, Kherani EA, Batista IS, MacDougall JW, Sobral JHA (2015) Wave structure and polarization electric field development in the bottomside F layer leading to postsunset equatorial spread F. J Geophys Res 120:6930. https://doi.org/10.1002/2015JA021235

Alex S, Koparkar PV, Rastogi RG (1989) Spread F and ionization anomaly belt. J Atmos Terr Phys 51:371

Batista IS, Abdu MA, Bittencourt JA (1986) Equatorial F region vertical plasma drifts: seasonal and longitudinal asymmetries in the American sector. J Geophys Res 91:12055

Bernhardt PA, Siefring CL (2006) New satellite based systems for ionospheric tomography and scintillation region imaging. Radio Sci 41:RS5S23. https://doi.org/10.1029/2005RS003360

Bittencourt JA, Abdu MA (1981) A theoretical comparison between apparent and real vertical ionization drift velocities in the equatorial F region. J Geophys Res 86:2451

Clemesha BR, Wright RWH (1966) A survey of equatorial spread F. In: Newman P (ed) Agardograph 95:3Spread F and its effects upon radio wave propagation and communications. W. and J. MacKay and Co., Ltd, London

Crain DJ, Heelis RA, Bailey GJ (1993) Effects of electrical coupling on equatorial ionospheric plasma motions: when is the F region a dominant driver in the low-latitude dynamo? J Geophys Res 98:6033

Dabas RS, Singh L, Lakshmi DR, Subramanyam P, Chopra P, Garg SC (2003) Evolution and dynamics of equatorial plasma bubbles: relationships to E × B drift, postsunset total electron content enhancements, and equatorial electrojet strength. Radio Sci 38:1075. https://doi.org/10.1029/2001RS002586

de La Beaujardiere O, the C/NOFS Science Definition Team (2004) C/NOFS: a mission to forecast scintillations. J Atmos Solar-Terr Phys 66:1573–1591

Dungey JW (1956) Convective diffusion in the equatorial F region. J Atmos Terr Phys 9:304

Eccles JV (1998a) A simple model of low-latitude electric fields. J Geophys Res 103:26,699

Eccles JV (1998b) Modeling investigation of the evening prereversal enhancement of the zonal electric field in the equatorial ionosphere. J Geophys Res 103:26,709

Eccles JV (2004) Assimilation of global-scale and mesoscale electric fields from low-latitude satellites. Radio Sci 39:RS1S09. https://doi.org/10.1029/2002RS002810

Eccles JV, Maynard N, Wilson G (1999) Study of the evening plasma drift vortex in the low-latitude ionosphere using San Marco electric field measurements. J Geophys Res 104:28133

Eccles JV, St Maurice JP, Schunk RW (2015) Mechanisms underlying the prereversal enhancement of the vertical plasma drift in the low-latitude ionosphere. J Geophys Res 120:4950. https://doi.org/10.1002/2014JA020664

Fagundes PR, Sahai Y, Batista IS, Abdu MA, Bittencourt JA, Takahashi H (1999) Observations of day-to-day variability in precursor signatures to equatorial F-region plasma depletions. Ann Geophys 17:1053

Farley DT, Balsley BB, Woodman RF, McClure JP (1970) Equatorial spread F: implications of VHF radar observations. J Geophys Res 75:7199

Farley DT, Bonelli E, Fejer BG, Larsen MF (1986) The prereversal enhancement of the zonal electric field in the equatorial ionosphere. J Geophys Res 91:13723

Fejer BG, de Paula ER, Batista IS, Bonelli E, Woodman RF (1989) Equatorial F region vertical plasma drifts during solar maxima. J Geophys Res 94:12,049

Fejer BG, de Paula ER, Gonzalez SA, Woodman RF (1991) Average vertical and zonal F region plasma drifts over Jicamarca. J Geophys Res 96:13901

Fejer BG, Farley DT, Gonzales CA, Woodman RF, Calderon C (1981) F region east-west drifts at Jicamarca. J Geophys Res 86:215

Fejer BG, Scherliess L, de Paula ER (1999) Effects of the vertical plasma drift velocity on the generation and evolution of equatorial spread F. J Geophys Res 104:19859

Fesen C, Crowley G, Roble RG, Richmond AD, Fejer BG (2000) Simulation of the pre-reversal enhancement in the low latitude vertical ion drifts. Geophys Res Lett 27:1851

Fukao S, Ozawa Y, Yamamoto M, Tsunoda RT (2003) Altitude-extended equatorial spread F observed near sunrise terminator over Indonesia. Geophys Res Lett 30:2137. https://doi.org/10.1029/2003GL018383

Fukao S, Yokoyama T, Tayama T, Yamamoto M, Maruyama T, Saito S (2006) Eastward traverse of equatorial plasma plumes observed with the equatorial atmosphere radar in Indonesia. Ann Geophys 24:1411

Gentile LC, Burke WJ, Rich FJ (2006) A global climatology for equatorial plasma bubbles in the topside ionosphere. Ann Geophys 24:163

Guzdar PN, Satyanarayana P, Huba JD, Ossakow SL (1982) Influence of velocity shear on the Rayleigh-Taylor instability. Geophys Res Lett 9:547

Guzdar PN, Satyanarayana P, Huba JD, Ossakow SL (1983) Correction. Geophys Res Lett 10:492

Haerendel G, Eccles JV (1992) The role of the equatorial electrojet in the evening ionosphere. J Geophys Res 97:1181

Haerendel G, Eccles JV, Cakir S (1992) Theory for modeling the equatorial evening ionosphere and the origin of the shear in the horizontal plasma flow. J Geophys Res 97:1209

Heelis RA (2004) Electrodynamics in the low and middle latitude ionosphere: a tutorial. J Atmos Solar-Terr Phys 66:825

Hoang TL, Abdu MA, MacDougall J, Batista IS (2010) Longitudinal differences in the equatorial spread *F* characteristics between Vietnam and Brazil. Adv Space Res 45:351

Huang CS, Kelley MC (1996a) Nonlinear evolution of equatorial spread F, 1. On the role of plasma instabilities and spatial resonance associated with gravity wave seeding. J Geophys Res 101:283

Huang CS, Kelley MC (1996b) Nonlinear evolution of equatorial spread F, 3. Plasma bubbles generated by structured electric fields. J Geophys Res 101:303

Jayachandran PT, Sri Ram P, Somayajulu VV, Rama Rao PVS (1997) Effect of equatorial ionization anomaly on the occurrence of spread F. Ann Geophys 15:255

Kelley MC, Larsen MF, La Hoz C, McClure JP (1981) Gravity wave initiation of equatorial spread F: a case study. J Geophys Res 86:9087

Klostermeyer J (1978) Nonlinear investigation of the spatial resonance effect in the nighttime equatorial F region. J Geophys Res 83:3753

Kudeki E, Bhattacharyya S (1999) Postsunset vortex in equatorial F-region plasma drifts and implications for bottomside spread-F. J Geophys Res 104:28163

Kudeki E, Fejer BG, Farley DT, Ierkic HM (1981) Interferometer studies of equatorial F region irregularities and drifts. Geophys Res Lett 8:377

Li G, Ning B, Abdu MA, Wan W, Hu L (2012) Precursor signatures and evolution of post-sunset equatorial spread-F observed over Sanya. J Geophys Res 117: A08321. https://doi.org/10.1029/2012JA017820

Li G, Otsuka Y, Ning B, Abdu MA, Yamamoto M, Wan W, Liu L, Abadi P (2016) Enhanced ionospheric plasma bubble generation in more active ITCZ. Geophys Res Lett 43:2389. https://doi.org/10.1002/2016GL068145

Makela JJ, Miller ES (2008) Optical observations of the growth and day-to-day variability of equatorial plasma bubbles. J Geophys Res 113:A03307. https://doi.org/10.1029/2007JA012661

Makela JJ, Vadas SL, Muryanto R, Duly T, Crowley G (2010) Periodic spacing between consecutive equatorial plasma bubbles. Geophys Res Lett 37: L14103. https://doi.org/10.1029/2010GL043968

Maruyama T (1996) Modeling study of equatorial ionospheric height and spread F occurrence. J Geophys Res 101:5157

Maruyama T, Kawamura M (2006) Equatorial ionospheric disturbance observed through a transequatorial HF propagation experiment. Ann Geophys 24:1401

Maruyama T, Nozaki K, Yamamoto M, Fukao S (2002) Ionospheric height changes at two closely separated equatorial stations and implications in spread F onsets. J Atmos Sol-Terr Phys 64:1557. https://doi.org/10.1016/S1364-6826(02)00093-7

Maruyama T, Saito S, Kawamura M, Nozaki K (2008) Thermospheric meridional winds as deduced from ionosonde chain at low and equatorial latitudes and their connection with midnight temperature maximum. J Geophys Res 113: A09316. https://doi.org/10.1029/2008JA013031

Maruyama T, Saito S, Kawamura M, Nozaki K, Krall J, Huba JD (2009) Equinoctial asymmetry of a low-latitude ionosphere-thermosphere system and equatorial irregularities: evidence for meridional wind control. Ann Geophys 27:2027

McClure JP, Singh S, Bamgboye DK, Johnson FS, Kil H (1998) Occurrence of equatorial F region irregularities: evidence for tropospheric seeding. J Geophys Res 103:29119

Narayanan VL, Taori A, Patra AK, Emperumal K, Gurubaran S (2012) On the importance of wave-like structures in the occurrences of equatorial plasma bubbles: a case study. J Geophys Res 117:A01306. https://doi.org/10.1029/2011JA017054

Ogawa T, Otsuka Y, Shiokawa K, Saito A, Nishioka M (2006) Ionospheric disturbances over Indonesia and their possible association with atmospheric gravity waves from the troposphere. J Meteor Soc Japan 84A:327

Otsuka Y, Shiokawa K, Ogawa T, Yokoyama T, Yamamoto M, Fukao S (2004) Spatial relationship of equatorial plasma bubbles and field-aligned irregularities observed with an all-sky airglow imager and the equatorial

Tsunoda *et al. Progress in Earth and Planetary Science* (2018) 5:22

Page 27 of 28

atmosphere radar. Geophys Res Lett 31:L20802. https://doi.org/10.1029/2004GL020869

Oya H, Takahashi T, Morioka A, Miyaoka H (1982) Wavy patterns of ionospheric electron density profiles triggered by TID – observation results of the electron density by TAIYO satellite. J Geomagn Geoelectr 34:509

Patra AK, Taori A, Chaitanya PP, Sripathi S (2013) Direct detection of wavelike spatial structure at the bottom of the F region and its role on the formation of equatorial plasma bubble. J Geophys Res 118:1196. https://doi.org/10.1002/jgra.50148

Prakash S, Pallamraju D, Sinha HSS (2009) Role of equatorial ionization anomaly in the development of the evening prereversal enhancement of the equatorial zonal electric field. J Geophys Res 114:A02301. https://doi.org/10.1029/2007JA012808

Raghavarao R, Hoegy W, Spencer NW, Wharton LE (1993) Neutral temperature anomaly in the equatorial thermosphere—a source of vertical winds. Geophys Res Lett 20:1023

Raghavarao R, Nageswararao M, Sastri JH, Vyas GD, Sriramarao M (1988) Role of equatorial ionization anomaly in the initiation of equatorial spread F. J Geophys Res 93:5959

Rastogi RG (1978) On the equatorial spread F. Proc Indian Acad Sci 87A:115

Rastogi RG, Patil A, Alex S (1991) Post-sunset uplifting of the equatorial F layer of the ionosphere and vertical plasma drift velocities. J Geomagn Geoelectr 43:607

Richmond AD, Fang TW, Maute A (2015) Electrodynamics of the equatorial evening ionosphere: 1. Importance of winds in different regions. J Geophys Res 120:2118. https://doi.org/10.1002/2014JA020934

Rishbeth H (1971) Polarization fields produced by winds in the equatorial F region. Planet Space Sci 19:357

Rodrigues FS, Crowley G, Heelis RA, Maute A, Reynolds A (2012) On the TIE-GCM simulation of the evening equatorial plasma vortex. J Geophys Res 117:A05307. https://doi.org/10.1029/2011JA017369

Röttger J (1973) Wave-like structures of large-scale equatorial spread-F irregularities. J Atmos Terr Phys 35:1195

Röttger J (1976) The macro-scale structure of equatorial spread-F irreglarities. J Atmos Terr Phys 38:97

Röttger J (1977) Travelling disturbances in the equatorial ionosphere and their association with penetrative cumulus convection. J Atmos Terr Phys 39:987

Röttger J (1981) Equatorial spread-F by electric fields and atmospheric gravity waves generated by thunderstorms. J Atmos Terr Phys 43:453

Saito S, Fukao S, Yamamoto M, Otsuka Y, Maruyama T (2008) Decay of 3-m-scale ionospheric irregularities associated with a plasma bubble observed with the equatorial atmosphere radar. J Geophys Res 113:A11318. https://doi.org/10.1029/2008JA13118

Saito S, Maruyama T (2006) Ionospheric height variations observed by ionosondes along magnetic meridian and plasma bubble onsets. Ann Geophys 24:2991

Saito S, Maruyama T (2007) Large-scale longitudinal variation in ionospheric height and equatorial spread F occurrences observed with ionosondes. Geophys Res Lett 34:L16109. https://doi.org/10.1029/GL030618

Sastri JH (1998) On the development of abnormally large postsunset upward drift of equatorial F region under quiet geomagnetic conditions. J Geophys Res 103:3983

Sastri JH, Meena Varma VK, Probhakaran Nayar SR (1995) Height gradient of F region vertical drift in the evening ionosphere. Geophys Res Lett 22:2645

Satyanarayana P, Guzdar PN, Huba JD, Ossakow SL (1984) Rayleigh-Taylor instability in the presence of a stratified shear layer. J Geophys Res 89:2945

Scannapieco AJ, Ossakow SL (1976) Nonlinear equatorial spread F. Geophys Res Lett 3:451

Schunk RW, Demars HG (2003) Effect of equatorial plasma bubbles on the thermosphere. J Geophys Res 108:1245. https://doi.org/10.1029/2002JA009690

Sekar R, Kelley MC (1998) On the combined effects of vertical shear and zonal electric field patterns on nonlinear equatorial spread F evolution. J Geophys Res 103:20,735

Sekar R, Raghavarao R (1987) Role of vertical winds on the Rayleigh-Taylor instabilities of the night time equatorial ionosphere. J Atmos Solar Terr Phys 49:981

Sekar R, Suhasini R, Raghavarao R (1994) Effects of vertical winds and electric fields in the nonlinear evolution of equatorial spread F. J Geophys Res 99:2205

Singh S, Johnson FS, Power RA (1997) Gravity wave seeding of equatorial plasma bubbles. J Geophys Res 102:7399

Sridharan R, Pallam Raju D, Raghavarao R, Ramarao PVS (1994) Precursor to equatorial spread F in OI 630.0 nm dayglow. Geophys Res Lett 21:2797

Su SY, Chao CK, Liu CH (2008) On monthly/seasonal/longitudinal variations of equatorial irregularity occurrences and their relationship with the postsunset vertical drift velocities. J Geophys Res 113:A05307. https://doi.org/10.1029/2007JA012809

Su SY, Wu CL, Liu CH (2014) Correlation between the global occurrences of ionospheric irregularities and deep atmospheric convective clouds in the intertropical convergence zone (ITCZ). Earth Planets Space 66:134

Thampi SV, Ravindran S, Pant TK, Devasia CV, Sreelatha P, Sridharan R (2006) Deterministic prediction of post-sunset ESF based on the strength and asymmetry of EIA from ground based TEC measurements: preliminary results. Geophys Res Lett 33:L13103. https://doi.org/10.1029/2006GL026376

Thampi SV, Ravindran S, Pant TK, Devasia CV, Sridharan R (2008) Seasonal dependence of the 'forecast parameter' based on the EIA characteristics for the prediction of equatorial spread F (ESF). Ann Geophys 26:1751

Thampi SV, Tsunoda R, Jose L, Pant TK (2012) Ionogram signatures of large-scale wave structure and their relation to equatorial spread F. J Geophys Res 117:A08314. https://doi.org/10.1029/2012JA017592

Thampi SV, Yamamoto M, Tsunoda RT, Otsuka Y, Tsugawa T, Uemoto J, Ishii M (2009) First observations of large-scale wave structure and equatorial spread F using CERTO radio beacon on the C/NOFS satellite. Geophys Res Lett 36:L18111. https://doi.org/10.1029/2009GL039887

Tsunoda RT (1980) On the spatial relationship of 1-m equatorial spread F irregularities and plasma bubbles. J Geophys Res 85:185

Tsunoda RT (1981) Time evolution and dynamics of equatorial backscatter plumes, 1, growth phase. J Geophys Res 86:139

Tsunoda RT (1983) On the generation and growth of equatorial backscatter plumes. 2. Structuring of the west walls of upwellings. J Geophys Res 88:4869

Tsunoda RT (1985) Control of the seasonal and longitudinal occurrence of equatorial scintillations by the longitudinal gradient in integrated E region Pedersen conductivity. J Geophys Res 90:447

Tsunoda RT (2005) On the enigma of day-to-day variability in equatorial spread F. Geophys Res Lett 32:L08103. https://doi.org/10.1029/2005GL022512

Tsunoda RT (2007) Seeding of equatorial plasma bubbles with electric fields from an E_s-layer instability. J Geophys Res 112:A06304. https://doi.org/10.1029/2006JA012103

Tsunoda RT (2008) Satellite traces: an ionogram signature for large-scale wave structure and a precursor for equatorial spread F. Geophys Res Lett 35:L20110. https://doi.org/10.1029/2008GL035706

Tsunoda RT (2009) Multi-reflected echoes: another ionogram signature of large-scale wave structure. Geophys Res Lett 36:L01102. https://doi.org/10.1029/2008GL036221

Tsunoda RT (2010a) On seeding equatorial spread F during solstices. Geophys Res Lett 37:L05102. https://doi.org/10.1029/2010GL042576

Tsunoda RT (2010b) On seeding equatorial spread F: circular gravity waves. Geophys Res Lett 37:L10104. https://doi.org/10.1029/2010GL043422

Tsunoda RT (2010c) On equatorial spread F: establishing a seeding hypothesis. J Geophys Res 115:A12303. https://doi.org/10.1029/2010JA015564

Tsunoda RT (2015) Upwelling: a unit of disturbance in equatorial spread F. Prog Earth Planet Sci 2. https://doi.org/10.1186/s40645-015-0038-5

Tsunoda RT, Baron MJ, Owen J, Towle DM (1979) ALTAIR: an incoherent scatter radar for equatorial spread F studies. Radio Sci 14:1111

Tsunoda RT, Bubenik DM, Thampi SV, Yamamoto M (2010) On large-scale wave structure and equatorial spread F without a post-sunset rise of the F layer. Geophys Res Lett 37:L07105. https://doi.org/10.1029/2009GL042357

Tsunoda RT, Ecklund WL (2007) On the post-sunset rise of the equatorial F layer and superposed upwellings and bubbles. Geophys Res Lett 34:L04101. https://doi.org/10.1029/2006GL028832

Tsunoda RT, Livingston RC, McClure JP, Hanson WB (1982) Equatorial plasma bubbles: vertically elongated wedges from the bottomside F layer. J Geophys Res 87:9171

Tsunoda RT, Livingston RC, Rino CL (1981) Evidence of a velocity shear in bulk plasma motion associated with the post-sunset rise of the equatorial F layer. Geophys Res Lett 8:807

Tsunoda RT, Maruyama T, Tsugawa T, Yokoyama T, Ishii M, Nguyen TT, Ogawa T, Nishioka M (2016a) Off-great-circle paths in transequatorial propagation, 1 discrete and diffuse types. J Geophys Res 121:11157. https://doi.org/10.1002/2015JA021695

Tsunoda *et al. Progress in Earth and Planetary Science* (2018) 5:22

Page 28 of 28

Tsunoda RT, Maruyama T, Tsugawa T, Yokoyama T, Ishii M, Nguyen TT, Ogawa T, Nishioka M (2016b) Off-great-circle paths in transequatorial propagation, 2. Non-magnetic-field-aligned reflections. J Geophys Res 121:11176. https://doi.org/10.1002/2016JA022404

Tsunoda RT, Nguyen TT, Le MH (2015) Effects of tidal forcing, conductivity gradient, and active seeding, on the climatology of equatorial spread F over Kwajalein. J Geophys Res 120:632. https://doi.org/10.1002/2014JA020762

Tsunoda RT, Thampi SV, Nguyen TT, Yamamoto M (2013) On validating the relationship of ionogram signatures to large-scale wave structure. J Atmos Solar-Terr Phys 103:30

Tsunoda RT, White BR (1981) On the generation and growth of equatorial backscatter plumes—1. Wave structure in the bottomside F layer. J Geophys Res 86:3610

Tsunoda RT, Yamamoto M, Tsugawa T, Hoang TL, Tulasi Ram S, Thampi SV, Chau HD, Nagatsuma T (2011) On seeding, large-scale wave structure, equatorial spread F, and scintillations over Vietnam. Geophys Res Lett 38:L20102. https://doi.org/10.1029/2011GL049173

Tulasi Ram S, Yamamoto M, Tsunoda RT, Chau HD, Hoang TL, Damtie B, Wassaie M, Yatini CY, Manik T, Tsugawa T (2014) Characteristics of large-scale wave structure observed from African and Southeast Asian longitudinal sectors. J Geophys Res 119:2288. https://doi.org/10.1002/2013JA019712

Tulasi Ram S, Yamamoto M, Tsunoda RT, Thampi SV (2012) On the application of differential phase measurements to study the zonal large scale wave structure (LSWS) in the ionospheric electron content. Radio Sci 47:RS2001. https://doi.org/10.1029/2011RS004870

Uemoto J, Maruyama T, Saito S, Ishii M, Yoshimura R (2010) Relationships between pre-sunset electrojet strength, pre-reversal enhancement and equatorial spread-F onset. Ann Geophys 28:449

Vadas SL (2007) Horizontal and vertical propagation and dissipation of gravity waves in the thermosphere from lower atmospheric and thermospheric sources. J Geophys Res 112:A06305. https://doi.org/10.1029/2006JA011845

Weber EJ, Basu S, Bullett TW, Valladares C, Bishop G, Groves K, Kuenzler H, Ning P, Sultan PJ, Sheehan RE, Araya J (1996) Equatorial plasma depletion precursor signatures and onset observed at 11° south of the magnetic equator. J Geophys Res 101:26829

Weber EJ, Buchau J, Eather RH, Mende SB (1978) North-south aligned equatorial airglow depletions. J Geophys Res 83:712

Whitehead JD (1971) Ionization disturbances caused by gravity waves in the presence of an electrostatic field and background wind. J Geophys Res 76:238

Woodman RF (1970) Vertical drift velocities and east-west electric fields at the magnetic equator. J Geophys Res 75:6249

Yokoyama T, Fukao S, Yamamoto M (2004) Relationship of the onset of equatorial F region irregularities with the sunset terminator observed with the Equatorial Atmosphere Radar. Geophys Res Lett 31:L24804. https://doi.org/10.1029/2004GL021529

Zalesak ST, Ossakow SL (1980) Nonlinear equatorial spread F: spatially large bubbles resulting from large horizontal scale initial perturbations. J Geophys Res 85:2131

Zalesak ST, Ossakow SL, Chaturvedi PK (1982) Nonlinear equatorial spread F: the effect of neutral winds and background Pedersen conductivity. J Geophys Res 87:151